Mechanisms of ocean heat uptake along and across isopycnals

Article

Published Version

It is advisable to refer to the publisher's version if you intend to cite from the work. See Guidance on citing.

To link to this article DOI: http://dx.doi.org/10.1175/JCLI-D-21-0793.1

Publisher: American Meteorological Society

www.reading.ac.uk/centaur

CentAUR

Mechanisms of Ocean Heat Uptake along and across Isopycnals

Louis Clément,[a] E. L. McDonagh,[b,a] J. M. Gregory,[c,d] Q. Wu,[c] A. Marzocchi,[a] J. D. Zika,[e,f,g] and A. J. G. Nurser[a]

[a] National Oceanography Centre, Southampton, United Kingdom
[b] Norwegian Research Centre (NORCE), Bjerknes Centre for Climate Research, Bergen, Norway
[c] National Centre for Atmospheric Science, University of Reading, Reading, United Kingdom
[d] Met Office Hadley Centre, Exeter, United Kingdom
[e] School of Mathematics and Statistics, University of New South Wales, Sydney, Australia
[f] UNSW Data Science Hub (uDaSH), University of New South Wales, Sydney, New South Wales, Australia
[g] Australian Centre for Excellence in Antarctic Science, University of New South Wales, Sydney, New South Wales, Australia

ABSTRACT: Warming of the climate system accumulates mostly in the ocean and discrepancies in how this is modeled contribute to uncertainties in predicting sea level rise. In this study, regional temperature changes in an atmosphere–ocean general circulation model (HadCM3) are partitioned between excess (due to perturbed surface heat fluxes) and redistributed (arising from changing circulation and perturbations to mixing) components. In simulations with historical forcing, we first compare this excess–redistribution partitioning with the spice and heave decomposition, in which temperature anomalies enter the ocean interior either along isopycnals (spice) or across isopycnals (heave, without affecting the temperature–salinity curve). Second, heat and salinity budgets projected into thermohaline space naturally reveal the mechanisms behind temperature change by spice and heave linked with water mass generation or destruction. Excess warming enters the ocean as warming by heave in subtropical gyres whereas it mainly projects onto warming by spice in the Southern Ocean and the tropical Atlantic. In subtropical gyres, Ekman pumping generates excess warming as confirmed by Eulerian heat budgets. In contrast, isopycnal mixing partly drives warming and salinification by spice, as confirmed by budgets in thermohaline space, underlying the key role of salinity changes for the ocean warming signature. Our study suggests a method to detect excess warming using spice and heave calculated from observed repeat profiles of temperature and salinity.

KEYWORDS: Ocean circulation; Ocean dynamics; Water masses/storage; Climate change; Climate variability; Heat budgets/fluxes; Ocean models

1. Introduction

Up to 93% of anthropogenic warming resulting from the increased concentrations of greenhouse gases since the 1950s is stored in the ocean (Rhein et al. 2013), reducing atmospheric warming. The absorption of excess heat (Levitus et al. 2012) that results from anthropogenic warming contributes through thermal expansion to sea level rise (Church et al. 2011). Prediction of sea level rise remains poorly constrained due to large uncertainties of ocean heat uptake (Kuhlbrodt and Gregory 2012) and its regional distribution. The absorption of heat anomalies at midlatitudes is believed to involve along-isopycnal transport, subsequent to subduction by Ekman convergence and geostrophic circulation (Stommel 1979; Church et al. 1991), or to involve an advective–diffusive vertical balance (Munk and Wunsch 1998). This first picture underlines the importance of shallow wind-driven subtropical gyres in heat transport (Talley 2013; Ferrari and Ferreira 2011) and of the adiabatic ventilated thermocline theory (Luyten et al. 1983). Furthermore, the mid-depth cell of the global overturning circulation (Talley 2013) reinforces the along-isopycnal

picture of temperature anomalies ventilated at high latitudes. In this adiabatic cell, density-compensated anomalies of North Atlantic Deep Water (NADW) flow southward along isopycnals (Mauritzen et al. 2012) and water parcels upwell also along isopycnals in the Southern Ocean (Marshall and Speer 2012). Recent investigations in general circulation models identified the reduction of high-latitude convection and advection in the Southern Ocean as the dominant processes responsible for the ocean heat uptake in CO_2 perturbed experiments (Exarchou et al. 2015; Kuhlbrodt et al. 2015).

Under anthropogenic forcing, ocean heat uptake is partly a passive process that follows water-mass ventilation pathways as depicted by Church et al. (1991). Simulations of temperature anomalies as a passive tracer allow estimation of redistributive anomalies, calculated in models from the residual between total temperature anomalies and the passive tracer (Banks and Gregory 2006; Marshall et al. 2015). Redistributive anomalies largely arise from the changing circulation—due to anthropogenic forcing—of the preindustrial temperature gradient. The decreased Atlantic meridional circulation generates the strongest redistribution warming (cooling) in the subtropical (subpolar) North Atlantic (Lowe and Gregory 2006;

Xie and Vallis 2012; Winton et al. 2013). Redistribution warming also occurs in tropical regions and in the Southern Ocean (Chen et al. 2019; Dias et al. 2020) contrasting with a prevalent passive warming of the Southern Ocean (Armour et al. 2016; Gregory et al. 2016). In addition, shallow redistribution cooling generates an extra warming by surface fluxes referred to as redistribution feedback (Garuba and Klinger 2016). Once added to the passive anomaly temperature tracer, this feedback forms the excess heat with its deepest penetration in the subpolar North Atlantic (Gregory et al. 2016). Recent efforts distinguish excess and redistributive heat in observations using the water mass transformation framework (Zika et al. 2021) or the similarity between the global ocean uptake of heat and carbon (Bronselaer and Zanna 2020).

The spice and heave framework (Bindoff and McDougall 1994) has been used to differentiate the role of air–sea fluxes onto subducted along-isopycnal properties from isopycnal displacements, due either to changes in water mass formation or to dynamical wind-driven changes, in hydrographic sections. Despite being influenced by natural variability, this decomposition revealed strong and equivalent (in temperature and salinity) subsurface patterns likely due to anthropogenic changes and believed to subduct along-isopycnals in large observational datasets of salinity (Durack and Wijffels 2010) and temperature (Häkkinen et al. 2016). The major driver of subducted anomalies often remains difficult to identify, being potentially forced by surface fluxes (Wong et al. 1999), by lateral movement of isopycnal in regions of changing surface properties (Lago et al. 2016), or by anomalies subducting on fixed lighter isopycnals (Church et al. 1991). Often, spice anomalies are considered to be influenced by surface buoyancy forcing and therefore to penetrate isopycnally below the mixed layer whereas deep transport of properties could also contribute to spice, for example by reducing along-isopycnal upward diffusive transport in the Southern Ocean (Gregory 2000). Another limitation is that global analyses often consider temperature and salinity separately. However, there is evidence that considering both together could inform as to whether spice trends preferentially result from anomalous heat fluxes in subtropical regions (in "alpha" oceans that are mostly stratified in temperature and where salinity is mostly passive; Durack and Wijffels 2010; Carmack 2007) or from high-latitude regions governed mainly by freshwater fluxes (in "beta" oceans that are mostly stratified in salinity and where temperature becomes mostly passive; Mauritzen et al. 2012).

In addition, the water mass transformation framework being in temperature–salinity space can be used to analyze the process-based heat and salinity tendency terms and to link them with the spice and heave decomposition. This framework allowed Walin (1982) to estimate the across-isothermal formation rate of water masses defined in temperature space using surface heat fluxes in the North Atlantic. Such a framework was extended to temperature–salinity space by Speer (1993), who depicts the intensity and direction of water mass transformation due to surface buoyancy forcing as a transformation vector. Moreover, Hieronymus et al. (2014) estimated the effect of subsurface mixing terms on the water mass formation rate. The water mass framework was also applied in

density space (Speer and Tziperman 1992) to reveal the predominance of along-isopycnal processes for heat uptake (Saenko et al. 2021).

In this study, using a coupled model in a climate change experiment with historical forcing, we first relate excess and redistributive heat to along-isopycnal (density-compensated) temperature anomalies (spice) or to diapycnal warming and water mass readjustment, both resulting in isopycnal displacements (heave). Then, Eulerian heat budgets unveil the mechanisms responsible for regional excess and redistribution warming. Finally, projecting heat and salinity budgets in S–θ space helps to detect which physical process produces warming by spice or heave and, therefore, helps to mechanistically relate the spice and heave decomposition with excess warming.

2. Methods

a. Temperature decomposition in excess and redistribution

In this study, excess heat (resulting from air–sea flux perturbations) is distinguished from redistributed heat. The latter primarily results from oceanic circulation changes and mixing perturbations under increasing atmospheric CO_2. We analyze the uptake of excess heat under realistic historical anthropogenic CO_2 forcing. Comparable experiments have previously been done with idealized scenarios of yearly 2% CO_2 increase (Banks and Gregory 2006) or with an abrupt CO_2 increase in ocean-only runs (Xie and Vallis 2012; Garuba and Klinger 2016).

We use the coupled atmosphere–ocean climate model HadCM3 (Hadley Centre Coupled Model version 3). Following the methodology of Banks and Gregory (2006), HadCM3 simulates excess heat as a passive anomaly temperature tracer. HadCM3 (Gordon et al. 2000) comprises a rigid-lid ocean model with a horizontal resolution of $1.25° \times 1.25°$ and with 20 unevenly spaced depth levels. The model was spun up for 800 years in the control experiment and a small climate drift was subtracted. Assuming that the drift has no nonlinear effect on the evolution, we consider a steady state for the control heat balance.

We evaluate the time-mean preindustrial surface heat flux $\overline{Q}$ over the last 150 years of the control experiment (Fig. 1a), in which the temperature θ follows under the Boussinesq approximation

$$c\frac{\partial \overline{\theta}}{\partial t} = \overline{Q} - \nabla \cdot (c\overline{v}\overline{\theta} + \overline{\phi}), \tag{1}$$

with the constant c being $\rho_0 c_p$ with a reference density $\rho_0 = 1026$ kg m^{-3} and the specific heat capacity $c_p = 3998$ J kg^{-1} K^{-1}; the overline denotes the unperturbed control steady state. The last term of the equations (ϕ) represents the nonadvective parameterized subgrid-scale processes of the ocean interior—that is, the isopycnal (ϕ_{iso}) and diapycnal (ϕ_{dia}) diffusion as well as the vertical mixing terms (ϕ_{vm}), which contains both the convective and mixed layer terms. The advective term (with the transport v) comprises the Eulerian and the GM eddy-induced advection. The subgrid-scale Gent–McWilliams (GM; Gent and McWilliams 1990)
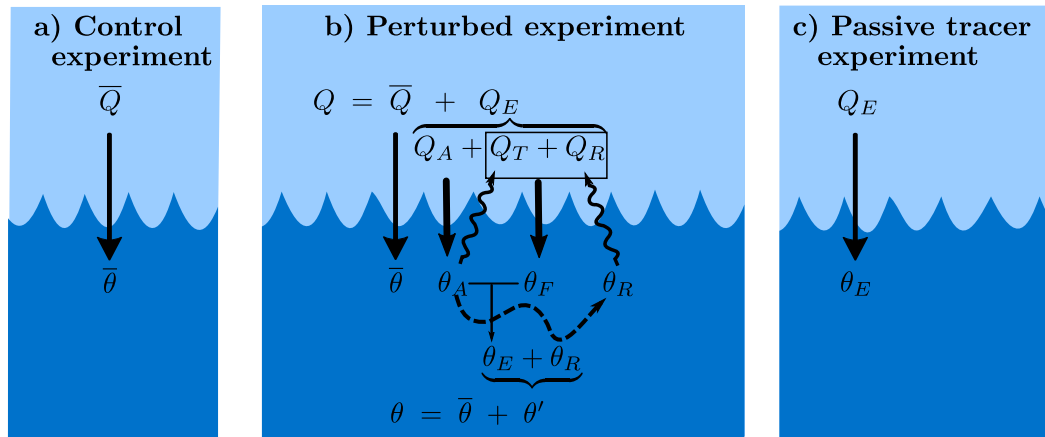
FIG. 1. (a) In the preindustrial control experiment, the surface boundary condition of ocean potential temperature $\theta = \overline{\theta}$ is the surface heat flux $\overline{Q}$. (b) In the perturbed experiment, the surface boundary condition of $\theta = \overline{\theta} + \theta'$ is $\overline{Q} + Q_E$, where θ' is the effect of climate change on ocean potential temperature, and Q_E is the sum of heat flux forcing Q_A and heat flux feedback. As well as being added to θ, and thus forcing climate change, the added heat flux Q_A is the surface boundary flux for the passive added heat tracer θ_A, which is initially zero and purely diagnostic. Climate change alters the SST (the surface field of θ) and consequently changes the surface heat flux. We distinguish two surface heat flux feedbacks. The direct feedback Q_T is the response of the atmosphere to the SST change caused by Q_A. The redistribution feedback Q_R arises from the change θ_R in ocean temperature, and hence in SST, due to redistribution of the control ocean heat content by modified ocean heat transports. The sum of surface heat flux feedbacks $(Q_T + Q_R)$ causes a change θ_F in ocean temperature. (c) In the passive tracer experiment, the surface excess heat flux $Q_E = Q_A$, and $\theta_E = \theta_A$, because Q_A is not added to θ, and hence there is no forced climate change. Once $\overline{\theta}$, θ, and θ_E are known, θ_R can be inferred.

eddy parameterization is implemented using the scheme of Visbeck et al. (1997) to preserve the spatial dependence of the eddy-induced diffusion coefficient. The Redi (1982) isopycnal diffusivity is implemented following the scheme of Griffies et al. (1998) with a constant along-isopycnal diffusion coefficient of 1000 m^2 s^{-1}. Within the mixed layer, the wind-energy mixing parameterization of Kraus and Turner (1967) is implemented whereas below the mixed layer, a depth-increasing vertical diffusivity of tracers linearly increases from its shallow background value of 0.1×10^{-4} m^2 s^{-1} to 1.22×10^{-4} m^2 s^{-1} at 4000 m following Pacanowski and Philander (1981). Furthermore, the convection scheme of Rahmstorf (1993) is implemented.

Following Exarchou et al. (2015), the Eulerian temperature tendency diagnostics (W m^{-3}) characterize the total heat flux convergence, which results either from varying heat uptake or heat transport processes. Similarly, salinity (S) tendency diagnostics (psu s^{-1}) are calculated with all diagnostics calculated monthly in Eulerian coordinates with E incorporating the effects of surface freshwater fluxes:

$$\frac{\partial \overline{S}}{\partial t} = \overline{E} - \nabla \cdot (\overline{v}\overline{S} + \overline{\phi}). \quad (2)$$

Beginning from the control state, a perturbed experiment (Fig. 1b) is run for 150 years with an added surface heat flux Q_A (Fig. 2a). This flux is time dependent, specified as monthly means starting in 1860, and is the perturbation to the local surface heat flux caused by the effective radiative forcing of the climate system, both anthropogenic and natural. It is diagnosed from the ECHAM6.3 atmosphere general circulation model with historically varying forcing agents and prescribed preindustrial sea surface climate (section 3.1 of Gregory et al. 2020) and thus does not include the response of the climate system (as described in the next paragraph). Quantities in the perturbed experiment are denoted without an overline, and primes denote the anomalies of the perturbed experiment relative to the control experiment. Thus $v = \overline{v} + v'$ and $\theta = \overline{\theta} + \theta'$ in the perturbed experiment. We use time-averaged variables over the last 50 years of the perturbed experiment (from 1960 to 2011) relative to the control experiment to quantify the temperature anomalies throughout our analysis.

The temperature of the perturbed experiment θ is forced at the surface by $Q = \overline{Q} + Q_E$, while a separate passive tracer θ_E, called "excess heat," initialized as zero, is forced by Q_E alone. The "excess surface heat flux" $Q_E = Q_A + Q_T + Q_R$ is the sum of the imposed added heat flux Q_A and the response $Q_T + Q_R$ of the climate system to the imposed flux. The redistribution feedback heat flux Q_R represents the heat flux change due to the sea surface temperature change arising from the movement of the background temperature by the circulation change (Garuba and Klinger 2016). The transport responsible for the circulation changes contains the advective terms as well as the diffusive and mixing terms. In addition, the atmosphere responds to the temperature change θ_A due to the added surface heat flux through an additional heat flux: the atmospheric feedback Q_T that tends to oppose Q_A and to reduce Q_E to approximately a third of the radiative forcing
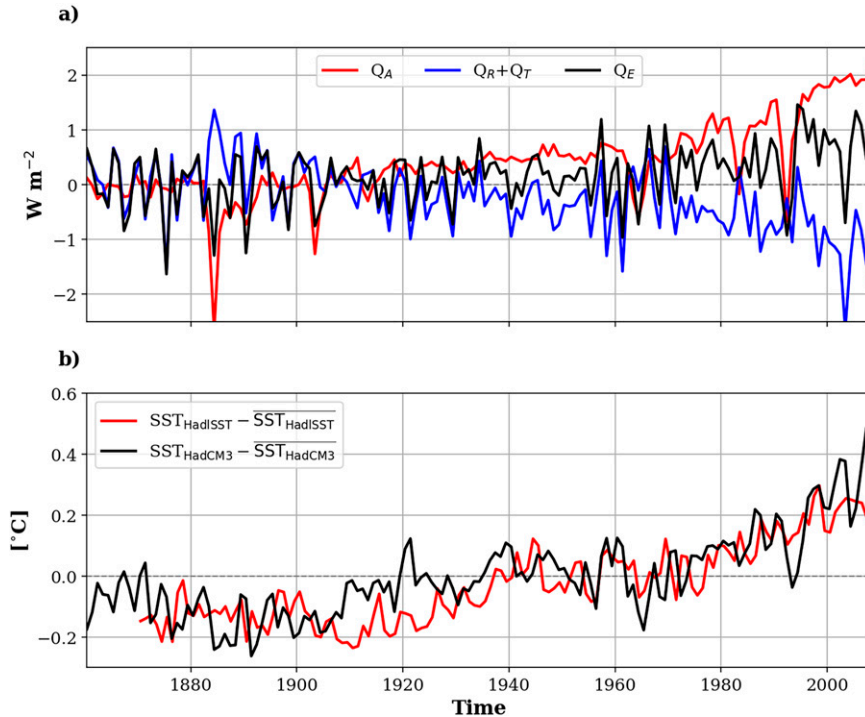
FIG. 2. (a) Global-mean excess surface heat flux Q_E (black), surface added heat flux Q_A (red), and sum of redistribution feedback Q_R and atmospheric feedback Q_T (blue). (b) Global-mean sea surface temperature relative to the full-period time average of the perturbed HadCM3 experiment and of the HadISST observations.

Q_A in the global mean (Kuhlbrodt and Gregory 2012). The excess heat θ_E, which is equivalent to the passive anomaly temperature [PAT in Banks and Gregory (2006)] follows

$$c\frac{\partial \theta_E}{\partial t} = Q_E - \nabla \cdot (c\overline{v}\theta_E + cv'\theta_E + \phi_E). \tag{3}$$

Using further passive tracers, we decompose $\theta' = \theta_E + \theta_R = \theta_A + \theta_F + \theta_R$, where the last three quantities are all initialized to zero, and their surface fluxes are Q_A, $Q_T + Q_R$, and zero respectively. The excess heat added by Q_A is θ_A, and θ_F is the excess heat due to the atmospheric feedbacks $Q_T + Q_R$. The redistributed heat θ_R arises from the effect of changing circulation and parameterized heat transports, and we calculate it as $\theta_R = \theta' - \theta_E$.

$$c\frac{\partial \theta_R}{\partial t} = -\nabla \cdot (cv'\overline{\theta} + c\overline{v}\theta_R + cv'\theta_R + \phi_R). \tag{4}$$

The heat redistribution integrated over the whole ocean is zero, which means that the global ocean heat content change relates to the total heat uptake through $\iiint c\theta' dV = \iiint c\theta_E dV = \iint Q_E dA$. By construction, the redistribution θ_R is unaffected by surface forcing while the redistributive surface heat fluxes $Q_T + Q_R$ only modify the excess heat.

Our experimental configuration differs from those of Gregory et al. (2016). For their heat-forced experiment FAF-heat they used method B of FAFMIP (the Flux-Anomaly-Forced Model

Intercomparison Project). Surface and atmospheric climate change is prevented in method B, except for redistribution feedback, so $Q_T = 0$ in the atmosphere–ocean heat flux. Instead, an estimate $\widehat{Q}_T$ is obtained from previous experiments, and included in the surface flux $Q_A + \widehat{Q}_T$ of "added heat." Since redistribution feedback is allowed to occur in method B, the flux of excess heat is $Q_E = Q_A + \widehat{Q}_T + Q_R$, the same as in our case with the replacement of Q_T by $\widehat{Q}_T$. However, Gregory et al. (2016) apply Q_R to θ_R, which therefore has a time-dependent ocean volume mean, instead of to θ_E. By contrast, in our method Q_R is included in the surface flux of θ_E, and our θ_R is "pure redistribution" whose surface flux is zero everywhere. In our experiment, all climate feedbacks are permitted in response to the imposed surface heat flux Q_A. The consequent climate change includes substantial changes to momentum and freshwater fluxes. Thus, the *results* of the experiment are more similar to those of FAF-all, in which all surface fluxes are perturbed, than to FAF-heat. On the other hand, our experiment is *technically* the same as FAFMIP FAF-heat method A, but that case has the substantially different surface flux $Q_A + \widehat{Q}_T$.

b. Spice and heave decomposition

Complementing the decomposition into excess and redistribution, which is model-based, we may also decompose temperature (and salinity) anomalies at each locations into their spice $\theta|_n$ and heave $\theta|_h$ components, following an observationally

motivated method (Bindoff and McDougall 1994). Spice relates to along-isopycnal temperature and salinity anomalies that are "density compensated" (i.e., with no net density change). Spice results from changes of air–sea fluxes where isopycnals outcrop and from changes in mixing processes along isopycnals. Heave, on the other hand, results from across-isopycnal anomalies and diabatic heat flux, due for example to diapycnal mixing or varying water mass formation, and also results from adiabatic water mass rearrangement, all of which are associated with isopycnal displacements. As done previously, the reference profile, denoted by overbars, is the depth average over the last 50 years of the control experiment and the anomaly with respect to this reference at constant depth is by definition

$$\theta'(t, z) = \theta(t, z) - \overline{\theta}(z) = \theta|_n(t, z) + \theta|_h(t, z). \quad (5)$$

Given the background density gradient $\partial\overline{\theta}/\partial\overline{\rho}$ and the density anomaly $\rho'(t, z)$, heave usually relies on the assumption of small isopycnal displacement, and by a Taylor approximation becomes (Bindoff and McDougall 1994)

$$\theta|_h(t, z) = \overline{\theta}[\rho(t, z)] - \overline{\theta}(z) \simeq \overline{\theta}[\overline{\rho}(z)] + \frac{\partial\overline{\theta}}{\partial\overline{\rho}}\rho'(t, z)$$

$$- \overline{\theta}[\overline{\rho}(z)] = \frac{\partial\overline{\theta}}{\partial\overline{\rho}}\rho'(t, z). \quad (6)$$

Rather than calculating heave, we instead use temperature and salinity profiles to calculate spice first, as an anomaly from the reference profile along isopycnals, and then infer heave as the remainder (Doney et al. 2007; Clément et al. 2020). This method removes the potential shallow residuals of the decomposition that can appear around the mixed layer when using the linearization of Eq. (6) applied to the background estimate of $\partial\overline{\theta}/\partial\overline{\rho}$ (Häkkinen et al. 2016)

$$\theta|_n(t, z) = \theta(t, z) - \overline{\theta}[\rho(t, z)], \quad (7)$$

$$\theta|_h(t, z) = \theta'(t, z) - \theta|_n(t, z) = \theta(t, z) - \overline{\theta}(z) - \theta|_n(t, z)$$

$$= \overline{\theta}[\rho(t, z)] - \overline{\theta}(z). \quad (8)$$

Calculations are done under the winter mixed layer (WML) base defined as the deepest mixed layer over the entire simulation (a definition that gives a unique value at each location).

c. Heat and salinity budgets in thermohaline coordinates

Extending the framework of Walin (1982), Speer (1993) expressed the water mass transformation (diabatic change of θ and S) due to surface forcing as vectors in S–θ space. Hieronymus et al. (2014) extended this representation by including the interior (diapycnal and isopycnal) mixing terms. The transformation vector is written $\mathbf{J} \equiv J^S(S, \theta), J^\theta(S, \theta)$. Here J^S has units of Sv °C^{-1} (1 Sv = 10^6 m^3 s^{-1}), so $J^S\Delta\theta$ represents the volume flux (in Sv) of water with temperature between θ and $\theta + \Delta\theta$ as it salinifies across the isohaline of salinity S, while J^θ has units of Sv per psu, so $J^\theta\Delta S$ represents the volume flux with

salinity between S and $S + \Delta S$ in Sv as water warms across the isotherm of temperature θ. The convergence of the transformation vector in S–θ space, integrated over finite ranges in θ and S, equals the formation rate (positive or negative) of water with properties in those ranges. This formation rate can be expressed either as a volume change or an outflow (if the transformation is evaluated over a limited domain). Hence, integrating over a "tube" of fluid with temperature ranging between θ and $\theta + \Delta\theta$, and salinity between S and $S + \Delta S$ with volume $v\Delta\theta\Delta S$, the diabatic convergence across the long sides of the tube produces a change in volume of $\partial v/\partial t\Delta\theta\Delta S$ and outflow $\Omega\Delta\theta\Delta S$ through the ends of the tube:

$$\frac{\partial v}{\partial t}\Delta\theta\Delta S + \Omega\,\Delta\theta\Delta S = -[J^S(S + \Delta S, \theta) - J^S(S, \theta)]\Delta\theta$$

$$- [J^\theta(S, \theta + \Delta\theta) - J^\theta(S, \theta)]\Delta S, \quad (9)$$

and taking the limit as $\Delta\theta \to 0$, $\Delta S \to 0$:

$$\frac{\partial v}{\partial t} + \Omega = -\frac{\partial J^S}{\partial S} - \frac{\partial J^\theta}{\partial \theta}; \quad (10)$$

here $\partial v/\partial t$ and Ω are denominated in units of Sv °C^{-1} psu^{-1}. The HadCM3 model that we diagnose in this paper only permits virtual salt fluxes at the surface, not mass fluxes of evaporation or precipitation, so surface mass fluxes cannot help balance the formation and the outflow term Ω drops out for global integrals.

The S and θ components of the transformation vector can be related to the material rate of change of S and θ (the total diabatic forcing) by a simple extension (Hieronymus et al. 2014) of standard one-property watermass theory (Walin 1982) according to

$$J^S = \lim_{\Delta S, \Delta\theta \to 0} \int_V \frac{DS}{Dt}\frac{\Pi(\theta - \theta')}{\Delta\theta}\frac{\Pi(S - S')}{\Delta S}\,dV, \quad (11)$$

$$J^\theta = \lim_{\Delta S, \Delta\theta \to 0} \int_V \frac{D\theta}{Dt}\frac{\Pi(\theta - \theta')}{\Delta\theta}\frac{\Pi(S - S')}{\Delta S}\,dV. \quad (12)$$

The calculation of J^S and J^θ involves the integration of the material rates of change over tubes with $|S - S'| < \Delta S/2$ and $|\theta - \theta'| < \Delta\theta/2$; this is expressed by the boxcar sampling function $\Pi(X - X') = 1$ for $|X - X'| < \Delta X/2$ and 0 otherwise.

The above formulas give the *total* transformation, but we can use Eqs. (1) and (2) to express the diabatic changes in terms of the forcing components:

$$\frac{DS}{Dt} = E + \phi_{iso}^S + \phi_{dia}^S + \phi_{vm}^S, \quad (13)$$

$$c\frac{D\theta}{Dt} = Q + \phi_{iso}^\theta + \phi_{dia}^\theta + \phi_{vm}^\theta, \quad (14)$$

and separate out the transformation resulting from different processes

$$\mathbf{J} = \mathbf{J}_{surf} + \mathbf{J}_{iso} + \mathbf{J}_{dia} + \mathbf{J}_{vm}, \quad (15)$$

where for example the contribution to the θ component of the transformation from isopycnal mixing is

$$J_{\text{iso}}^{\theta} = \lim_{\Delta S, \Delta\theta \to 0} \int_V c^{-1}\phi_{\text{iso}}^{\theta} \frac{\Pi(\theta - \theta')}{\Delta\theta}\frac{\Pi(S - S')}{\Delta S} dV.$$

When surface mass fluxes can be neglected and a global and sufficiently long time integral is taken such that the divergence in S–θ space is zero ($\nabla_{S\theta} \cdot \mathbf{J} \equiv \partial J^S/\partial S + \partial J^\theta/\partial\theta = 0$), $\mathbf{J}$ can be represented as a streamfunction (Döös et al. 2012; Zika et al. 2012). When both fluid velocity and local tracer tendencies are appropriately averaged, this streamfunction describes the flow across isotherms and isohalines (Groeskamp et al. 2014). A nonnegligible S–θ divergence is evident in our volume budget, which is likely partly associated with the numerical mixing resulting from the model's advection scheme (Holmes et al. 2019) and from errors in our diagnostics (e.g., due to offline averaging).

Finally, to link the thermohaline budgets with the decomposition presented in section 2b, we evaluate the contributions of the spice and heave components to the formation rates by projecting the transformation vectors from S–θ space into a space whose basis vectors lie along isopycnals and along S–θ curves (see the appendix), with $\mathbf{J} = \mathbf{J}_{\text{spice}} + \mathbf{J}_{\text{heave}}$.

3. Results

In this section, after introducing the atmospheric forcing, we compare the excess–redistribution and heave–spice decompositions for temperature. The heave–spice decomposition is also applied to salinity to reveal regional patterns of both heat and salinity budgets. Then, Eulerian heat budgets describe regionally the prevailing mechanisms behind excess–redistribution warming. Finally, heat and salinity budgets projected in thermohaline coordinates reveal the processes responsible for spice–heave warming, which can further be linked to excess warming using results of Eulerian heat budgets.

a. Atmospheric forcing

Our experiment aims to reproduce a realistic heat flux forcing under a historical CO_2 scenario. The time series of the global-mean surface heat fluxes (Fig. 2a) reflect the strong increase in surface added heat flux Q_A starting from the 1960s and partly compensated by the redistribution feedback Q_R and the atmospheric feedback Q_T. The global-mean excess surface heat flux Q_E averaged from 1960 to 2011 is 0.85 W m^{-2}. This heat flux somewhat overestimates a recent estimate of net heating, inferred from observed ocean heat content changes, of 0.52 W m^{-2} from 1960 to 2015 (Cheng et al. 2017) when averaged over the ocean's surface. Nonetheless, the model surface forcing simulates sea surface temperature SST anomalies that are sufficiently realistic for the purposes of our work, seeing that they reproduce well the decadal trends of observed SST anomalies (HadISST in Fig. 2b; Rayner et al. 2003) and their absolute increase over the past century. HadISST contains optimally interpolated SSTs from ship data until 1981 complemented by in situ and satellite SSTs from 1982. We note that

the AOGCM internally generates its own unforced interannual variability, which cannot be expected to replicate the historical record.

b. Decompositions of temperature anomalies

Contrasting the excess–redistribution and heave–spice temperature decompositions (shown zonally averaged in Fig. 3) underlines the varying patterns of ocean heat absorption along isopycnals at high latitudes (Figs. 3i,j) versus across isopycnals in subtropics (Figs. 3g,h). It also highlights the specific mixed regime of the Atlantic north of 20°S with strong warming both across and along isopycnals (Figs. 3h and 3j) and where increased salinity becomes prevalent (Fig. 4b).

Since the excess heat enters from the surface, its warming effect is strongest in the upper ocean. Excess heat generally causes warming above 700 m (Figs. 3c and 3d). The deepest penetration of excess warming occurs in the subpolar North Atlantic (>2500 m) whereas not much deep excess warming appears below 500 m for the rest of the ocean. The largest excess warming appears in the subpolar North Atlantic and in the subtropical South Atlantic (Fig. 3d). In these regions it is amplified by the redistribution feedback (i.e., the response to redistributive surface cooling; Fig. 3f), and the net excess warming mostly overcompensates the redistributive cooling.

Redistribution is an indirect result of the surface excess warming. Redistribution mostly cools the ocean above 700 m, except for some subsurface warming in the subtropics (Fig. 3f) and North Pacific (Fig. 3e), and warms the ocean below this depth, but only makes a negligible change to the globally integrated heat content (in conformance with its definition). Despite using larger heat fluxes resulting from their 4 × CO_2 scenario, Garuba and Klinger (2016) observed similar patterns of excess and redistributed heat.

In subtropical gyres above 700 m, except in the North Atlantic, heave captures most of the excess warming, probably conveyed from the surface by Ekman downwelling, while the redistributive cooling is mostly by spice (and must therefore be accompanied by freshening). In the North Atlantic, on the other hand, the excess warming due to redistribution feedback mostly projects onto spice above 500 m (Fig. 3j), and must be accompanied by salinification, while redistributive cooling at 30°N and 400 m with warming below (Fig. 3f) projects onto heave (Fig. 3h). In addition, weak warming by heave occurs below 500 m, which is redistribution likely arising from the reduced tropical upwelling due to a reduced overturning (Gregory 2000; Banks and Gregory 2006).

The spice patterns agree with previously observed cooling and freshening by spice in the gyres other than the North Atlantic, as well as the warming and salinification of the North Atlantic, over roughly similar periods (Durack and Wijffels 2010; Häkkinen et al. 2016). Equatorward of 30°N in the Atlantic, both heave and spice (Figs. 3h and 3j) explain some of the excess warming. Warming by heave in the North Atlantic has previously been related to heat transport convergence in both the subtropical and subpolar gyres (Williams et al. 2014;
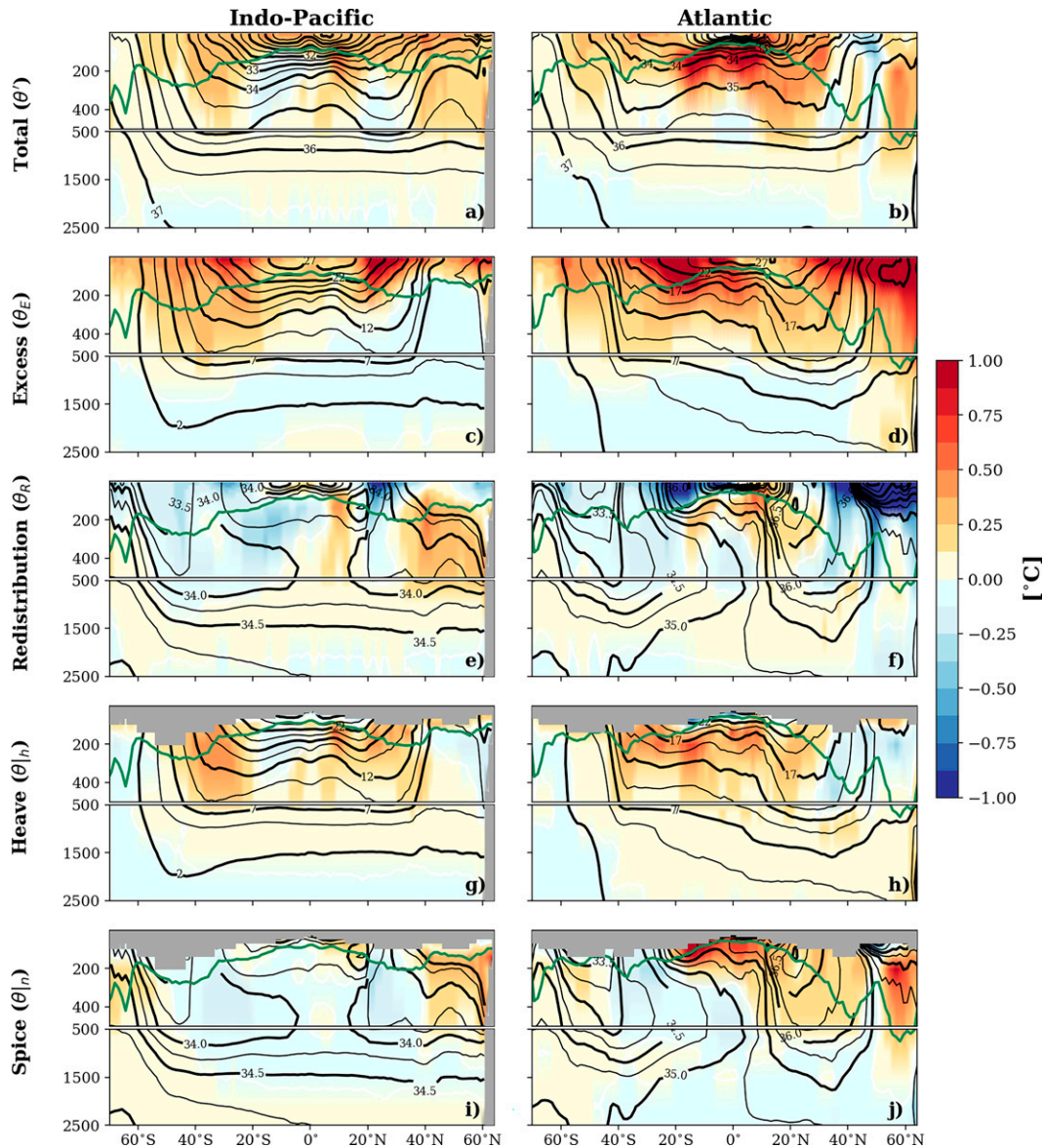
FIG. 3. (a),(b) Zonally averaged temperature anomalies for the (left) Indo-Pacific and (right) Atlantic and their decomposition into either (c),(d) excess and (e),(f) redistribution or into (g),(h) heave and (i),(j) spice. The WML base is indicated in green, but the variables are shown up to the shallowest winter mixed layer of 1961–2011 for heave and spice. Black contours indicate various time-averaged σ_2 isopycnals (in the first row), isotherms (second and fourth rows), and isohalines (third and fifth rows).

Häkkinen et al. 2015), but is present only in the subtropics in our experiment.

c. Temperature anomalies at the WML base

For understanding the uptake of heat under climate change, we are particularly interested in temperature anomalies associated with excess warming at the base of the winter mixed layer (WML). The WML base (Fig. 3) lies at around 200 m in the extratropics; it is shallower in the tropics (~50–100 m) and deeper in the North Atlantic (~300–500 m). At the WML base, except in the North Atlantic, excess warming and warming by heave

are similar in subtropical gyres (green and blue respectively in Figs. 5a and 5b; see also Fig. 3), while spice is associated with both positive and negative temperature change. However, in the tropical and North Atlantic, excess warming is predominantly by spice at the WML base (Fig. 5b). On the global mean, below the WML base, excess accounts for ~70% of the increased ocean heat content, leaving a substantial component of redistributed warming, while heave accounts for ~107%, which exceeds 100% because of global cooling by spice (Figs. 5c and 5d). Spice contributes little to the volume-integrated warming below ≈500 m where isopycnals flatten so
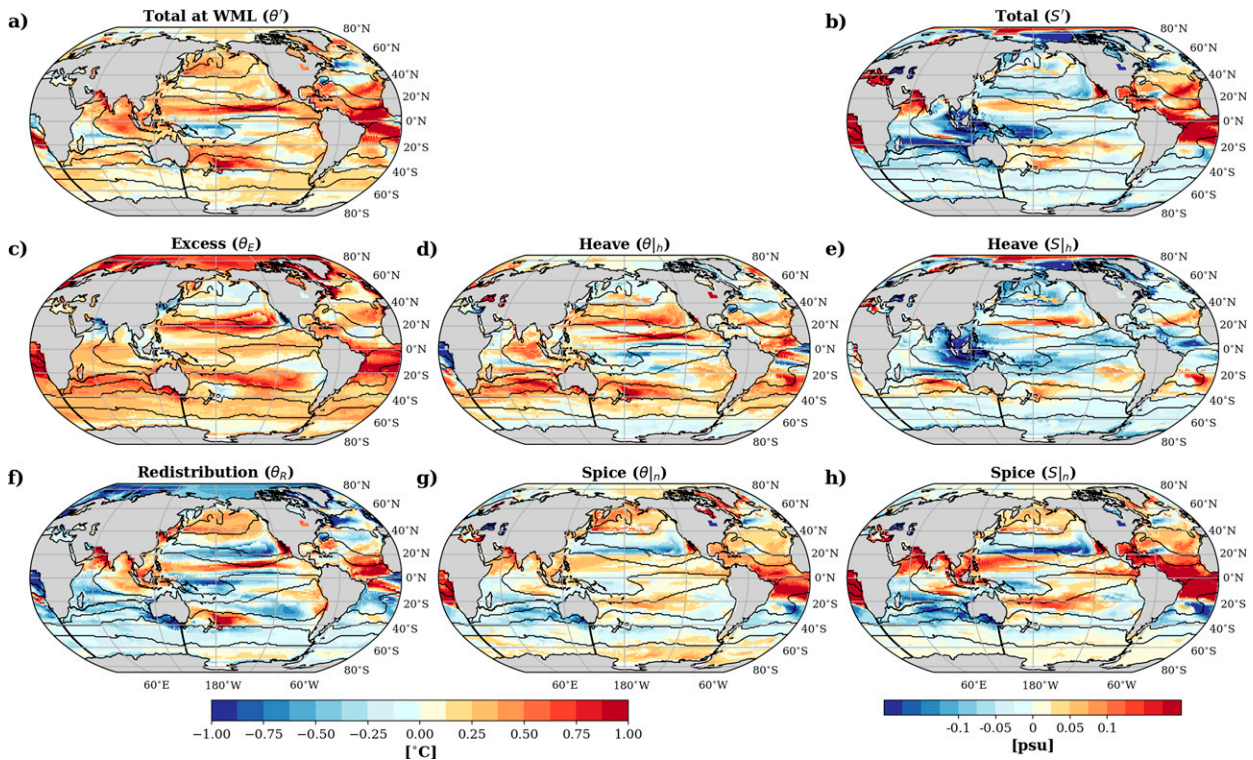
FIG. 4. (a) Total temperature anomalies over the past 50 years, decomposed into (c) excess and (f) redistribution and into (d) heave and (g) spice. (b) Total salinity anomalies, decomposed into (e) heave and (h) spice. Each component is shown at the WML base. The black contours delimit the surface patches that were used to estimate ocean heat content from boundary conditions at the sea surface (Zanna et al. 2019).

vertical diffusion (which imprints as heave) becomes relatively more important while spice cooling of subtropical gyres continues to be significant.

The basin-mean spice effect is warming at the WML base of the Atlantic and Indo-Pacific Oceans (0.21° and 0.07°C, respectively) but the volume-mean change in ocean heat content by spice (WML–2000 m; Figs. 5c and 5d) is weakly negative in both basins (-0.2 and -0.5×10^{22} J, respectively). This difference is strongest in the subtropical Atlantic where spice is associated with excess at the WML base (Fig. 5b), with a 2D spatial correlation coefficient R of 0.56 (and a p value < 0.01 as for all reported correlation coefficients) at 20°S–40°N, but spice does not predict excess below the WML base (Fig. 5d). In this region, there are peaks of warming at 10°S and 10°N (Fig. 4a), which are not features of excess warming by spice. In contrast, they coincide with maxima in heave and redistribution (Figs. 4d and 4f), which are strongly correlated in the subtropical Atlantic, at $R = 0.78$. As opposed to spice warming, the similarities between excess warming and warming by heave previously found in subtropical gyres (except the North Atlantic) persist at the WML base and below it, with $R = 0.58$ in the Atlantic around 40°–20°S below the WML base. The excess warming by heave is counteracted both at the WML base and below it by cooling by redistribution and spice, with $R = 0.75$ between them for the heat content in the same region of the Atlantic.

Whether temperature anomalies enter the ocean as anomalies that are density-compensated (spice) or not (heave) helps us to interpret long-term stratification changes over the top 2000 m (Figs. 5e and 5f) and changes of mixed layer depth (Figs. 5g and 5h). Ekman pumping of excess heat across (horizontal) isopycnals at the center of subtropical gyres projects onto heave, increases the stratification (e.g., by ~4%–7% at 30°S; Figs. 5e and 5f), and reduces the WML depth (Figs. 5g and 5h) in all but the North Pacific.

The behavior in the tropics and northern extratropics of the Atlantic is again unusual. There is a maximum of excess warming at the WML base of the Atlantic at 20°S–0° (Fig. 5b, green), which reflects strong intrusion into the ocean interior of heat due to redistribution feedback (not shown). As noted above, this warming is by spice (Fig. 5b, red), with strong imprints by spice in both temperature and salinity (Figs. 4a,b,g,h), and thus enters the ocean along isopycnals before being transported northward (Fig. 3j). This excess warming at 20°S–0° opposes the substantial shallow redistributive cooling, which is confined above the WML base (Fig. 3f). Acting together, these two effects deepen the WML base (Fig. 5h) and produce a subsurface maximum warming just below the WML base (Fig. 3b) and thus reduce the stratification (Fig. 5f), in a region where stratification is mostly affected by temperature. This region of strong shallow excess and spice warming agrees with the region of observed enhanced spice salinification in Fig. 7c of Durack and Wijffels (2010).
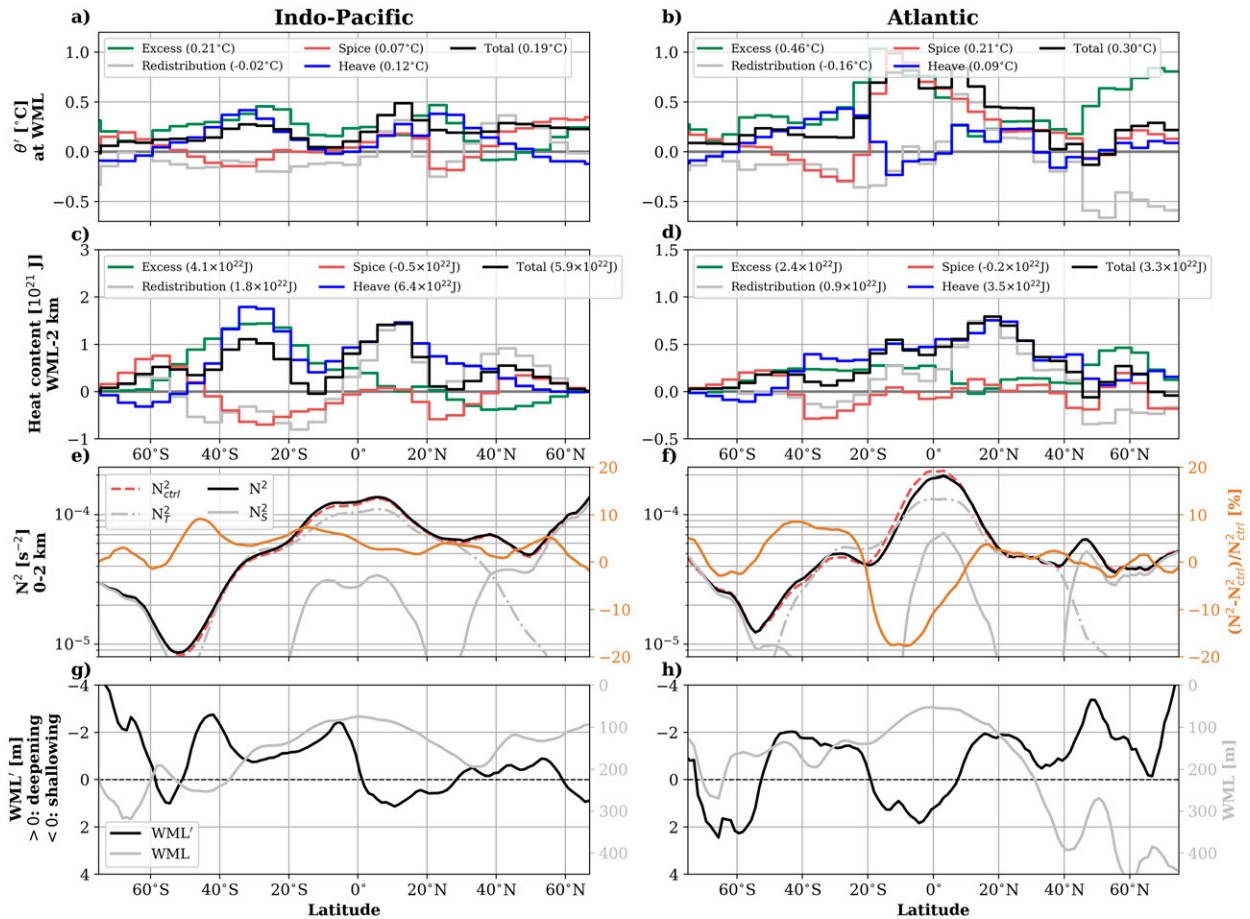
FIG. 5. Temperature anomalies (black) at the WML base decomposed into excess (green)/redistribution (gray) and heave (blue)/spice (red) zonally averaged across the (a) Indo-Pacific and (b) Atlantic with their meridional average indicated in labels. (c),(d) As in (a) and (b), but for zonally and depth-integrated heat content from the WML base to 2000 m with their volume integral indicated in labels. Stratification of the control (dashed red) and perturbed experiments (black) with its temperature (dashed gray) and salinity (gray) components for the (e) Indo-Pacific and (f) Atlantic. The percent difference in stratification of the perturbed relative to the control experiment is indicated in brown (right y axis). (g),(h) Difference (black; left y axis) between the WML base of the perturbed (gray; right y axis) and control experiments.

In the Labrador and Irminger Seas the combined area-integral subsurface heat content change is 33×10^{21} J due to excess warming, and 33×10^{21} J due to warming by spice. Because this strong excess heat uptake is almost entirely by spice, it has little effect on the density-driven circulation or redistribution (Fig. 4f), in agreement with observation (Mauritzen et al. 2012; Lozier et al. 2019; Zou et al. 2020).

In the Southern Ocean, south of subtropical gyres, warming by spice exceeds warming by heave; the latter decreases with increasing latitude to become negligible around 60°S (Figs. 3g–j). Excess warming occurs above ~400 m; redistributive warming below (Figs. 3c–f). The spatially averaged warming by spice of 0.14°C is similar to the excess warming at the WML base (Figs. 5a,b) south of 60°S. However, the spatial variability of warming by spice is negatively correlated with excess heat at the WML base ($R = -0.48$ south of 45°S) and positively correlated with redistributed heat ($R = 0.56$) as expected from Figs. 4f and 4g. Below the WML base, the correlation between

spice and redistribution is even stronger ($R = 0.80$ in the Indo-Pacific). Thus, in the Southern Ocean (around 60°S) spice captures both shallow excess and deep redistributive warming that are separated around the spatially varying WML base, discarding any strong correlation with spice at the WML base. Farther north (50°–40°S), however, heave captures most of the excess heat throughout the water column.

Having previously described the 2D spatial correlations, we investigate the large-scale correspondence between excess and spice–heave by comparing temperature anomalies spatially averaged over 26 surface patches (Fig. 6a). These patches were previously used to estimate ocean heat content from sea surface temperature assuming steady transport by a Green's function (Zanna et al. 2019). As expected, the strongest positive and significant correlation of $R = 0.88$ between the excess and heave is found mainly in subtropical gyres (Fig. 6b). For the southernmost patches (the three dark red markers in Fig. 6f) and the tropical Atlantic (light red triangles in Fig. 6f), the total
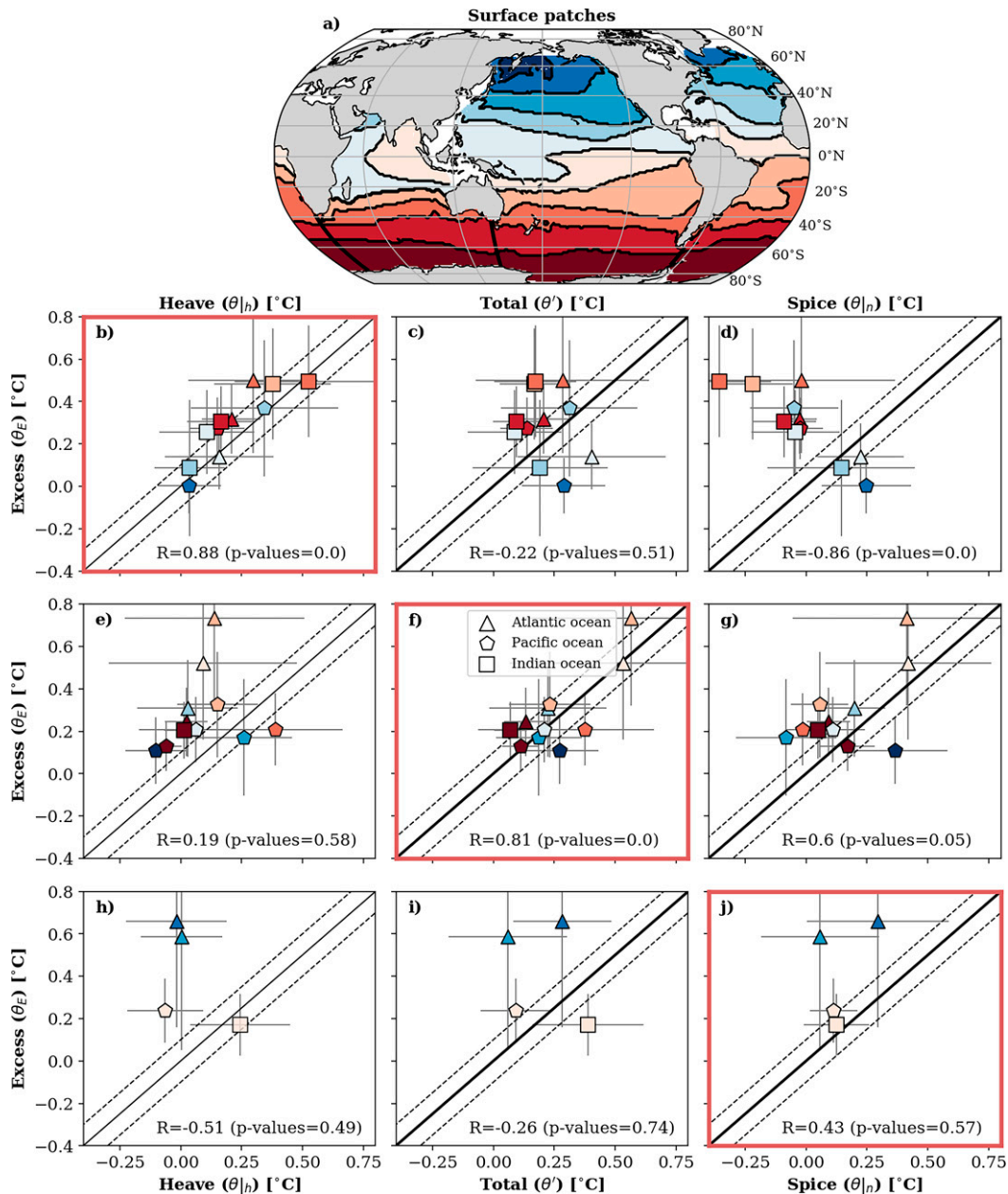
FIG. 6. (a) Surface patches that were used to estimate ocean heat content from boundary conditions at the sea surface (Zanna et al. 2019). Excess temperature anomalies spatially averaged for each patch (with the marker color corresponding to one patch) and displayed, vs (b),(e),(h) heave, (c),(f),(i) total temperature anomalies, and (d),(g),(j) spice; (b), (f), and (j) contain the patches where heave, total anomalies, and spice, respectively, are the closest to excess, providing the highest correlation coefficient R. Triangles, pentagons, and squares represent the surface patches of the Atlantic, Pacific, and Indian Oceans, respectively. Standard deviations are added in gray lines.

anomalies (spice + heave) best represent the excess. This underlines the small contribution of redistribution south of 60°S at the WML base. For the Labrador Sea patch (darkest blue triangle in Fig. 6j), spice best captures the excess warming although it remains half the size of excess. In the other patch of the subpolar Atlantic (lightest blue triangle in Fig. 6j), neither the spice nor heave captures the excess warming since the

strongest redistributed cooling (Fig. 4f) is unrepresented by the spice–heave decomposition and likely results from the weakening of the Atlantic MOC (Yin et al. 2010; Bouttes et al. 2014).

d. Decompositions of salinity anomalies

We investigate changes in salinity and also decompose them into their heave and spice components (Figs. 4e and 4h)
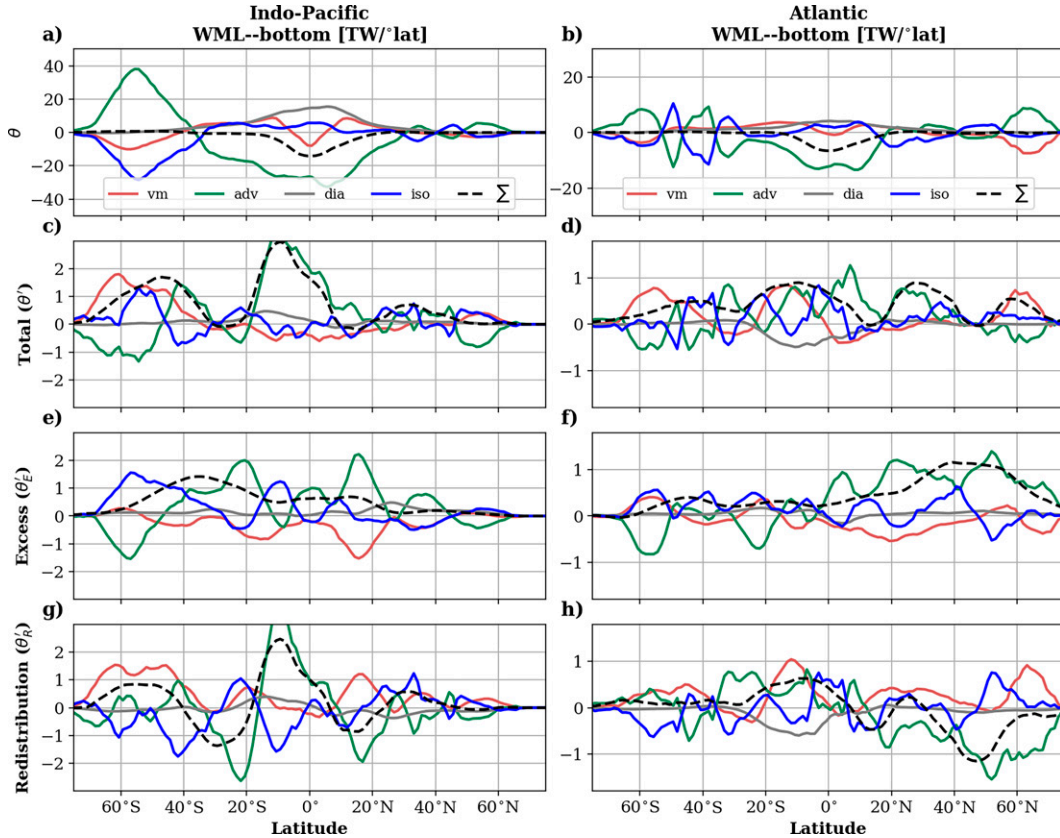
FIG. 7. Zonally and depth-integrated heat flux convergences below the WML base of the perturbed experiment for the (left) Indo-Pacific and (right) Atlantic: (a),(b) total temperature θ, (c),(d) temperature anomalies θ', (e),(f) excess θ'_E, and (g),(h) redistribution θ'_R.

to elucidate the role of along-isopycnal penetration in creating salinity anomalies and to reveal regional salinity trends, useful for interpreting the thermohaline budgets discussed below. Total and spice salinity intensify in the Atlantic with the deepest spice penetration in the North Atlantic but spice salinity freshens in the Indo-Pacific as expected from Figs. 3j and 3i. As opposed to temperature, within 40°S–40°N total salinity and its spice component are strongly correlated ($R = 0.81$), which underlines the prevalence of along-isopycnal salinity absorption also described in Lago et al. (2016).

Heave salinification (Fig. 4e) in regions of Ekman downwelling marks regions of maximal surface salinity for all subtropical gyres, which are mostly characterized by salinification (Fig. 4b). This heave salinification emphasizes the role of vertical advection that is also present in the North Atlantic along with the effects resulting from the weakened AMOC potentially captured by spice (Fig. 4h). Increased (decreased) salinity in the subtropical (subpolar) North Atlantic as well as the salinity pile-up in the South Atlantic potentially results from AMOC weakening (Levang and Schmitt 2020; Zhu and Liu 2020). The salinification of the subtropical/tropical Atlantic (Fig. 4b) with the global freshening of the Pacific at the WML base is consistent with the intensification of the water cycle in warmer scenarios (Levang and Schmitt 2015) associated with a more evaporative Atlantic and more precipitative Pacific.

e. Eulerian heat budgets

We now investigate Eulerian heat budgets depth-integrated below the WML base to identify the processes responsible for temperature anomalies and for the warming due to excess and redistributed heat. The heat budget is qualitatively similar in the control experiment (not shown) and the perturbed experiment (Figs. 7a and 7b), because there are large balancing terms in the control, and the perturbations are small by comparison. As previously described for a volume below 120 m in Exarchou et al. (2015), the Southern Ocean dominates the balance, with warming advection (ϕ^{θ}_{adv}, green) due to the large-scale circulation opposed by cooling eddy effects (isopycnal diffusion ϕ^{θ}_{iso}, in blue, and eddy advection, the latter being included in the net ϕ^{θ}_{adv} in Fig. 7) and by cooling convection (included in vertical mixing ϕ^{θ}_{vm}, red). In the tropics and subtropics, warming by diapycnal mixing (ϕ^{θ}_{dia}, gray) compensates advective cooling due to upwelling.

Away from the equator, two peaks of net heat uptake emerge at 45°S and 30°N in the difference of the perturbed experiment with respect to control (black dashed lines, Figs. 7c and 7d). Poleward of 40°, warming is dominated in both hemispheres by vertical mixing, with a contribution from isopycnal mixing in the Southern Hemisphere; these are due to relatively small reductions in the cooling due to the same
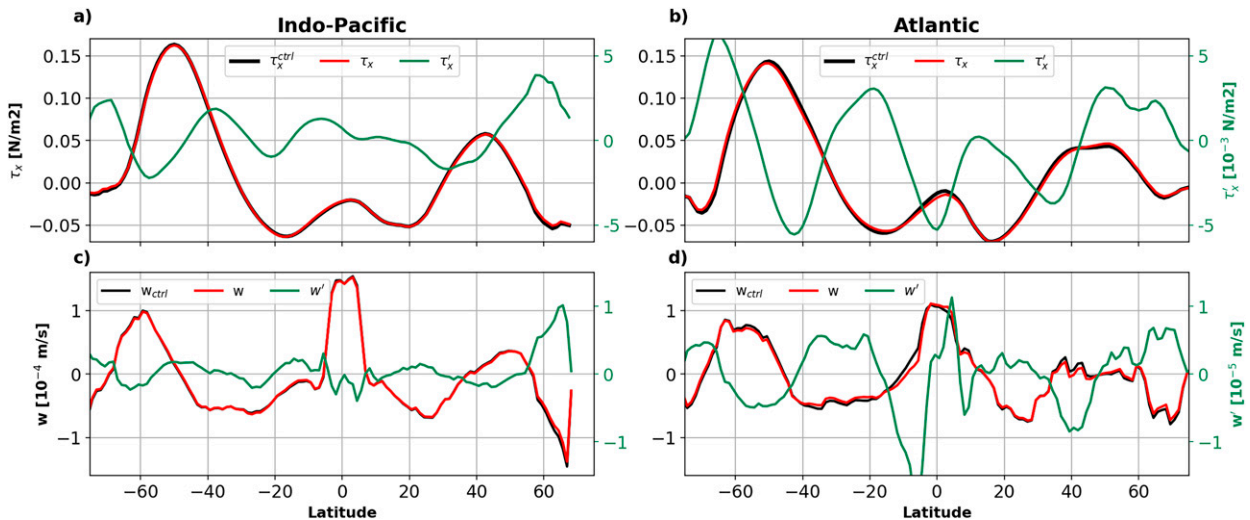
FIG. 8. Zonally averaged zonal wind stress τ_x for the perturbed (red) and control (black) experiments (left y axis) and their difference (green, right y axis) for the (a) Indo-Pacific and (b) Atlantic Oceans. (c),(d) As in (a) and (b), but for the vertical velocity depth-averaged from the surface to 500 m.

processes in the control. The warming due to vertical mixing around 60°S and 60°N is a redistribution due to reduced convective heat loss (Figs. 7g and 7h). With a warmer surface climate, or with increased surface freshwater flux, convection transports less heat upward, resulting in deep warming (Manabe et al. 1990), and also weakening the buoyancy-driven overturning circulation. The weakened overturning circulation and reduced easterlies (Fig. 8a) diminish the equatorial cold upwelling (Fig. 8c) and potentially warm the redistribution below 400–500 m (Fig. 3e) with a strong advective component (Fig. 7g) that is compensated by an advective full-depth excess cooling (not shown).

In addition to the convective parameterization, in the control experiment vertical mixing contains the wind-induced turbulent mixing that opposes and mixes surface fluxes while slightly warming below ~100 m (~500–1000 m) in equatorial (higher latitude) regions. These surface fluxes comprise the intensified cooling of the nonpenetrative component at the shallowest depth and the large warming of the shortwave component below (not shown). This large warming is compensated by the vertical mixing cooling that appears, for example, at 50°S (Fig. 7a) and that should be affected by changing winds.

In the perturbed experiments, the strengthening and lateral shift of the westerlies over the Southern Ocean affect both vertical mixing and advective terms in Exarchou et al. (2015). In our perturbed experiment, a lateral shift occurs in the Atlantic but without strengthening of the westerlies (Fig. 8b). Consistent with reduced cooling subsequent to the weakened westerlies at ~50°S (Figs. 8a and 8b), turbulent vertical mixing causes subsurface warming by downward redistribution of heat at ~45°–50°S (Figs. 7g and 7h) as further confirmed by analyzing the wind-mixing energy flux (not shown) that is strongly reduced at ~50°S. These weakened winds coupled with the increased westerlies (60°–65°S) prevail in the Atlantic

while occurring 5°–10° farther south than in Exarchou et al. (2015) and Morrison et al. (2016).

At 40°S in the Indo-Pacific, the westerlies to the south and easterlies to the north induce Ekman convergence and along-isopycnal downwelling of SAMW (Subantarctic Mode Water) and AAIW (Antarctic Intermediate Water) characterized by an advective warming peak (ϕ_{adv}^{θ}; in green, Fig. 7c). This peak comprises equal contributions from excess and redistribution (Figs. 7e and 7g). The wind-driven background circulation transports shallow warm temperature anomalies northward across isopycnals within the mixed layer (Rintoul and England 2002) and around the WML base as seen from the negative advective peak at 60°S (Figs. 7e and 7f). This process is most likely represented by the advective excess warming at 40°S (Fig. 7e) and has also been referred to as "passive advection" (Armour et al. 2016). These anomalies then enter the ocean interior along isopycnals below the mixed layer. The redistribution warming at 40°S results from the GM eddy advection perturbation (not shown separately from ϕ_{adv}^{θ}), which warms at depth and opposes the background eddy cooling of the control experiment.

Although the peaks of excess and redistributed warming by advection in the Indo-Pacific around 40°S should mostly project onto warming by spice as both being along isopycnals, warming by heave mostly prevails at 40°S (Figs. 3g and 3h) as would be expected from changes in water volumes resulting from wind-driven changes; for example, increased volumes of SAMW (Gao et al. 2018) and decreased volumes of AAIW. Our analysis is focused below the WML base and so may overemphasize this heave contribution while not fully capturing the shallow spice warming in this region due to the local deep WML base (~200 m).

In the Indo-Pacific subtropical gyres around 20°S/N (Figs. 7e and 7g), advective excess warming is mostly compensated by advective redistributed cooling, and the correspondences

heave–excess and spice–redistribution are strong (Fig. 5a). Along with this subtropical advective excess warming, salinification by heave in these regions (Fig. 4e), where S as well as θ increases toward the surface and where their anomalies are the strongest, indicates that heave is due to the background downward Ekman pumping of surface anomalies. In addition, weakened subtropical gyres support reduced Ekman downwelling, for example at 20°N in the Pacific (Fig. 8c), as previously noticed in increased CO_2 scenarios (Saenko et al. 2005). This anomalous upwelling causes the shallow redistributed cooling, which appears as spice (for reasons that remain to be elucidated).

In the North Atlantic, the weakening of the meridional overturning circulation reduces northward heat advection, thus giving redistributive advective warming (20°S–20°N) and cooling (20°–60°N) (Fig. 7h). The strong excess advective warming north of 20°N (Fig. 7f) is due to redistribution feedback. The excess warming (0°–20°N in Fig. 3d), which seems to be advective (Fig. 7f), projects onto both spice and heave (Figs. 3h and 3j). Spice under the WML base may depict the injection of temperature anomalies by the background and/or perturbed vertical circulation at outcropping isopycnals (20°S–0°), which corresponds to the region of highest surface (not shown) and subsurface salinity changes (Fig. 4b). Also in this region and in the North Atlantic with Ekman pumping similar to other subtropical gyres, heave captures the background cross-isopycnal excess heat change due to Ekman flux.

The perturbed isopycnal diffusion has a warming effect in the Southern Ocean around 50°S in the Indo-Pacific ($\phi_{\text{iso}}^{\theta}$ in blue; Fig. 7c), which opposes the cooling of the control experiment (Fig. 7a). Most of this isopycnal warming occurs in excess heat. It differs from a redistributed warming that would be expected with a reduced temperature gradient along sloping isopycnals that shoal poleward from deep warm to shallow colder waters (Gregory 2000). Therefore, along-isopycnal eddy stirring must contribute to the transport of the warm excess heat downward and equatorward instead of upward and poleward.

Redistributed diapycnal mixing warms in the Indo-Pacific around 0°–20°S ($\phi_{\text{dia}}^{\theta}$ in gray; Fig. 7g), as expected from the enhanced stratification (Fig. 5e) while it cools in the equatorial South Atlantic (Fig. 7h). This cooling is likely due to the sharp negative vertical gradient of redistributive temperature just below the WML base (Fig. 3f) that remains in total temperature anomalies (Fig. 3b), and that contributes to the reduced stratification (Fig. 5f).

f. Heat and salinity budgets of the control experiment in thermohaline coordinates

We now project heat and salinity budgets onto thermohaline coordinates with the aim of identifying the processes that generate warming by spice and heave for the perturbed experiment in the next section. Time-averaged total transformation vectors **J** are shown in Fig. 9e for the full global ocean in the control experiment and quantify the volume per unit time (in Sv) crossing an isotherm or an isohaline (by scaling **J** by

ΔS and $\Delta \theta$; see section 2c). The divergence $\nabla_{S\theta} \cdot \mathbf{J}$ (shading in Fig. 9e) in $S–\theta$ space gives the rates of water mass formation ($\nabla_{S\theta} \cdot \mathbf{J} < 0$) and destruction ($\nabla_{S\theta} \cdot \mathbf{J} > 0$) in the control experiment. The total transformation vectors **J** reflect the two main thermohaline cells described by Döös et al. (2012) and Zika et al. (2012): the shallow tropical Pacific cell at high temperature and the global conveyor cell that extends to NADW at lower temperature. These cells should have zero divergence, as they are calculated over the full global ocean, so there is no outflow Ω in Eq. (10) and the control experiment is in steady state after averaging over the seasonal cycle so the watermass volume v should not change. The nonzero divergence of these cells may arise partly from numerical mixing and partly from (mostly unavoidable) imperfection in our diagnostics.

The decomposition of the total transformation vectors for the full ocean into the contributions from the various forcing processes [Eq. (15)] shows that surface fluxes (Fig. 9a) generally spread water masses toward their $S–\theta$ boundaries (Nurser et al. 1999)—that is, warming warm waters and cooling cold waters and similarly freshening fresher waters and salinifying saltier waters—compensated by both isopycnal and diapycnal mixing terms (Figs. 9b and 9c) that concentrate water masses toward the center (i.e., warming cool waters and cooling warm waters). Note that isopycnal diffusion transforms waters along isopycnals (gray contours show σ_2), while diapycnal diffusion just operates vertically along the local $\theta–S$ curve and so has no preferred alignment relative to isopycnals. Convection and mixed-layer entrainment $\mathbf{J}_{\text{vm}}$ (Fig. 9d) is relatively unimportant, except for cooling at warm temperatures 25°–30°, likely associated with entrainment of upwelling equatorial waters in the Pacific, and warming of very cold waters associated with convection.

Restricting the budget to the volume below the WML base excludes most transformation above 20°–25°C (cf. Figs. 9j and 9e) and practically all the effects of surface fluxes (cf. Figs. 9f and 9a). Isopycnal and diapycnal mixing is much weakened (Figs. 9g and 9h), emphasizing the importance of mixing within the seasonal thermocline. However, the dipole of formation and destruction driven by isopycnal diffusion is evident in both the full and interior ocean (Figs. 9b and 9g) and the θ direction of **J** below the WML (Fig. 9g) corroborates the Eulerian heat balance (Figs. 7a and 7b), that is, mainly cooling in the Southern Ocean at low temperatures.

Flow out of this interior domain across the WML (obduction/ subduction) is now permitted and represents a positive/negative outflow Ω term in the mass balance [Eq. (10)], so, in the steady state, positive divergence $\nabla_{S\theta} \cdot \mathbf{J}$ in Fig. 9j may represent $\theta–S$ classes that lose mass through mixing in the thermocline, but are resupplied by net subduction, whereas negative divergences (convergences) may represent waters that gain mass through subsurface mixing and hence upwell (obduct) in the global sum. Caution is however required in interpreting these divergences, given the large spurious full-ocean divergences evident in Fig. 9e.
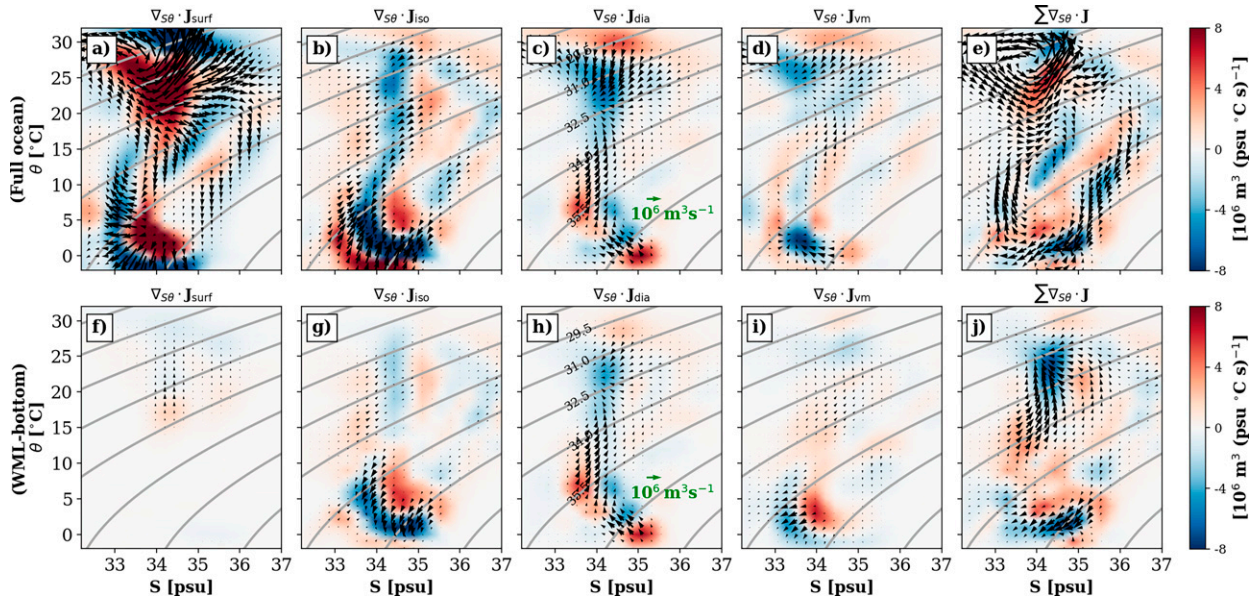
FIG. 9. Transformation vector **J** and its divergence for (a)–(e) the full ocean and (f)–(j) the volume below the WML base for the control experiment. Positive (negative) divergence denotes water mass destruction (formation). Each column represents the individual effect of the surface fluxes, the isopycnal and diapycnal mixing, and the vertical mixing; the last column represents the sum of all these effects. Gray lines denote σ_2 isopycnals surfaces labeled in (c) and (h).

g. *Perturbed experiment in thermohaline coordinates*

The anomalies in the total transformation **J′** and in water mass formation $\nabla_{S\theta} \cdot$ **J′** in the perturbed experiment relative to the control experiment are shown in Fig. 10 (rightmost panels) for the interior domain below the WML in various ocean basins (different rows). Note that because the ocean is evolving in the historical run, the volume balance [Eq. (10)] for S–θ tubes now includes inflation/deflation of the "tubes" (nonzero $\partial v/\partial t$); this inflation/deflation depends on the net inflow/outflow Ω through the WML base and any changes in it, as well as on the transformation below the WML that we describe here. In addition, we relate the changes in water mass formation rates to the spice and heave framework in Fig. 11 by decomposing the anomalies of the transformation vector into their components along isopycnals, **J′**$_{spice}$, and along S–θ curves, **J′**$_{heave}$ (see the appendix).

The strongest signals in the interior transformation of Fig. 10 are evident in the North and South Atlantic and the southern Indo-Pacific, involving warming and salinification at temperatures between 15° and 25°C, as expected from before in the subtropical regions, and a cooling/warming dipole in the South Atlantic and southern Indo-Pacific for temperatures below 10°C. The S–θ curves averaged over 20° latitude bands [i.e., 0°–20° (tropical), 20°–40° (subtropical), 40°–60° (subpolar), and 60°–80° (polar)] are drawn in Fig. 10 (rightmost panels) as dashed red curves for the perturbed run and black lines for the control. The longest curve in each basin is for the tropical band: the curves get shorter moving to subtropical, subpolar, and polar regions consistent with the cooler surface waters. The S–θ curves for subtropical regions

(where $10°C < \theta < \sim 20°C$) include the rightmost curve in the North Atlantic (Fig. 10d); the curve second to right in the South Atlantic (Fig. 10h), the middle curve in the northern Indo-Pacific (Fig. 10l), and the second from right in the southern Indo-Pacific (Fig. 10p). All these curves and the tropical curves (where $15°C < \theta < \sim 25°C$) show generally increasing θ and S toward the surface except in the southern Indo-Pacific (p).

In the North Atlantic, the warming and salinification below the WML occurring from $\theta = 15°C$ to $\sim 27°C$ (Fig. 10d) are primarily achieved by isopycnal mixing (Fig. 10a). This isopycnal warming emerges in the thermohaline representation but is not evident in the depth-integrated Eulerian heat budget of the North Atlantic (Fig. 7d). It presumably results from isopycnal fluxes down across the WML driven by warming and salinification at the surface, or from a potential meridional contribution of isopycnal mixing warming from the South Atlantic (Fig. 10e) as expected from Fig. 3j and 3d. The **J′** in the subtropics is decomposed into heave and spice (Fig. 11a) over the range $5°C < \theta < \sim 27°C$. Since the **J′** mostly results from isopycnal diffusion, it expresses as spice rather than heave [note the closeness of the red (spice) and black (total) arrows in Fig. 11a for high S]. Therefore, the water mass framework allows us to attribute a process of isopycnal warming to the shallow spice warming in the tropical Atlantic at 20°S–20°N (Fig. 3j), mainly linked to excess warming (Fig. 5b). Because this spice warming is reminiscent of observations (Durack and Wijffels 2010), we hypothesize that isopycnal warming by excess heat may contribute to these observations. Interestingly, low-latitude spice warming along horizontal isopycnals has the unexpected effect of reducing stratification and of increasing locally the WML base at 20°S–0° (Figs. 5f
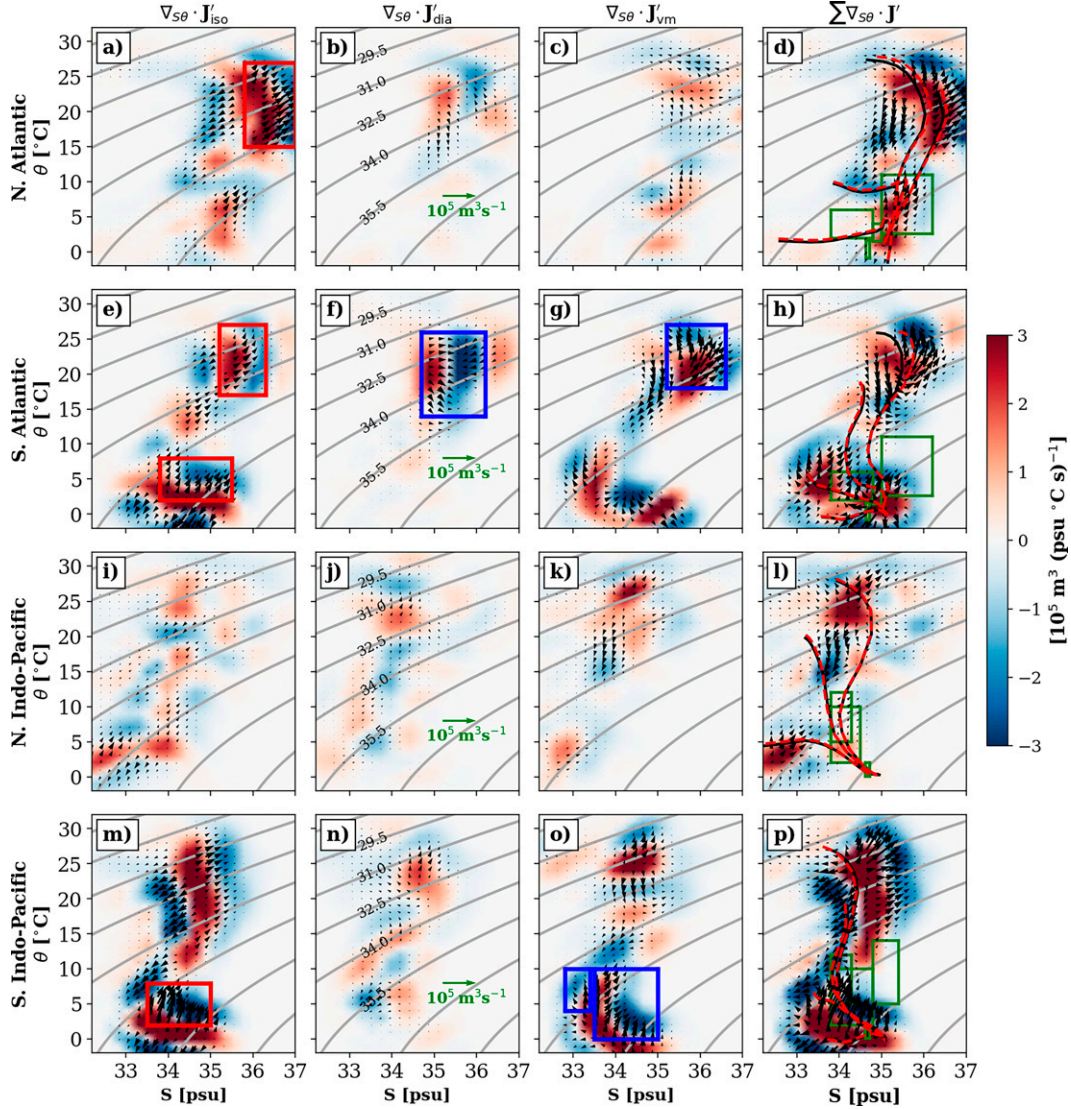
FIG. 10. Transformation vector of the anomalies **J′** and its divergence of the anomalies for (a)–(h) the North and South Atlantic and (i)–(p) the northern and southern Indo-Pacific below the WML base. The red and blue boxes represent predictions of excess and redistribution, respectively, based on zonal-averaged θ and S of Fig. 3. The S–θ curves in the last column are averaged across each 20° latitudinal band for the perturbed (dashed red line) and control experiments (black line). The green boxes in the last column delimit the intermediate and deep water masses (Emery 2001) from the freshest to saltiest in the Atlantic [AAIW, Antarctic Bottom Water (AABW), NADW, and MW] and in the Indo-Pacific [Pacific Subarctic Intermediate Water (PSIW), AAIW, Circumpolar Deep Water (CDW), and Red Sea–Persian Gulf Intermediate Water (RSPGIW)]. Gray lines denote σ_2 isopycnals surfaces labeled in the second column.

and 5h), contrasting with the expected stratification increase of subtropical and tropical regions in a warmer climate.

The picture for the cold waters in the Southern Ocean is different. Isopycnal warming and salinification occur over narrower salinity range $S \in [33.5, 35]$ psu and temperature range $\theta \in [2, 8]$°C (Fig. 10m) than vertical mixing warming (Fig. 10o) and, at the same time, over a smaller latitudinal range 45°–55°S (Fig. 7c) than vertical mixing warming at 45°–65°S. The strong along-isopycnal vertical mixing warming of the southern Indo-

Pacific (Fig. 10o) for $\theta \in [0, 10]$°C at high S should mainly represent the redistributive convective warming around 60°S (Fig. 7g) given that S increases with depth in this region (Fig. 3e). The relatively flat subpolar and polar S–θ curves in the region unambiguously indicate spice warming as confirmed for $\theta \in [0, 5]$°C and $S \sim 34.5$ psu in Figs. 11c and 11d. As a result, we conclude that spice warming at 60°S (Figs. 3i and 3j) below 300–400 m is most likely linked to redistributive warming due to reduced convection; spice warming at
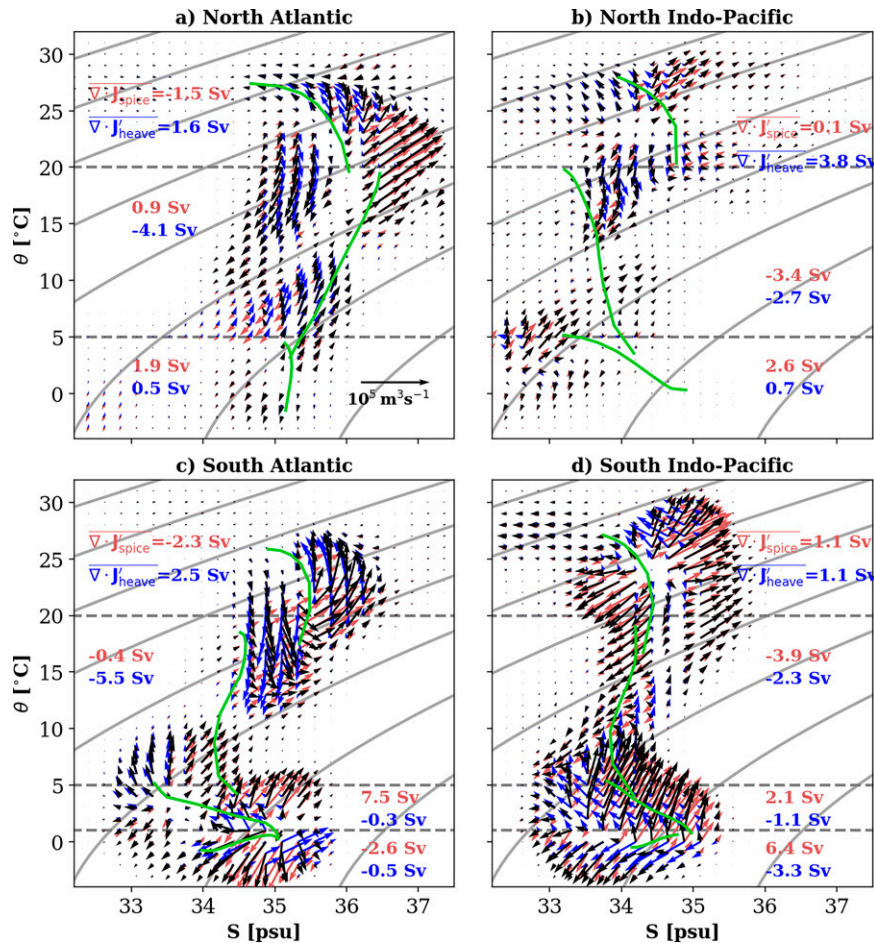
FIG. 11. Transformation vectors of the anomalies **J′** (black) and their decomposition in spice along isopycnals (red) and in heave along S–θ curves (blue) for the (a) North and (c) South Atlantic and for the (b) northern and (d) southern Indo-Pacific below the WML base. The S–θ divergence of the vector decomposition are summed in S–θ space ($\overline{\nabla \cdot \mathbf{J}'_{\text{spice}}}$ and $\overline{\nabla \cdot \mathbf{J}'_{\text{heave}}}$) for various temperature ranges and are indicated in the red (spice) and blue (heave) captions. These temperature ranges characterize regions of different S–θ curves that are delimited by the horizontal gray dashed lines. The S–θ curves (green) of the control experiment are averaged across each 20° latitudinal band and displayed individually for each temperature ranges. Gray lines denote σ_2 isopycnals.

50°S (Fig. 3i), however, is likely linked to excess warming by isopycnal mixing (Fig. 7c). In contrast, around similar $\theta \in [4, 10]$°C but for lower S (~33 psu), the wind-driven redistributive vertical mixing warming (Fig. 10o) related to the shifting of westerlies strongly projects onto heave warming as seen in Fig. 11d for the southern Indo-Pacific. Consequently, the shallow heave warming above 500 m at 50°–40°S (Figs. 3g and 3h) most likely results from a redistributive warming. Overall, both heave and spice components are important for these cold Southern Ocean waters (Figs. 11c,d) although spice only seems to capture some of the excess warming.

4. Conclusions

In this work, we study the processes of heat uptake during historical ocean climate change in a simulation using the HadCM3 AOGCM. Our aim is to make physical connections between the different views offered by model diagnostics and observationally motivated analysis techniques. HadCM3 is a typical AOGCM in its formulation; although it was developed more than 20 years ago, its simulations are within the range of and more realistic than some modern AOGCMs (Tett et al. 2022). Thus we expect our qualitative conclusions to apply to other AOGCMs, with quantitative differences, for instance due to the rather low vertical resolution of HadCM3 (20 depth layers) and systematic uncertainty in important model parameters (such as isopycnal diffusivity).

First, we identified regional similarities between two decompositions of temperature anomalies: the spice and heave decomposition and a partitioning arising either from perturbed surface heat fluxes (excess) or from perturbed circulation (redistribution). Second, Eulerian heat budgets revealed

the processes responsible for the excess and redistributed warming that, once associated with salinity budgets and projected into thermohaline space, allowed us to attribute the processes driving the warming by spice and heave. This attribution became possible in thermohaline space given the slopes of isopycnals and of S–θ curves and it revealed along-isopycnal warming patterns undetected in depth-integrated Eulerian heat budgets. This study addresses the patterns and potential drivers of oceanic temperature changes in different frameworks most often used for observations and models. Our work may help to distinguish in observations the contribution of excess heat to warming at the depth of the winter mixed layer base, which could be used in the future to initialize the boundary conditions of passive experiments (Khatiwala et al. 2013; Zanna et al. 2019).

Overall, the absorption of excess heat in the diabatic shallow circulation of the subtropical regions (stably stratified in temperature) occurs across isopycnals via Ekman downwelling and projects onto warming by heave. This relationship, present in all subtropical gyres, is further associated with a redistributive cooling and a cooling due to spice mainly in the Indo-Pacific, and which seems to be associated with a decreased downward Ekman volume flux. In equatorial regions, subsurface across-isopycnal heave warming characterizes the decreased overturning circulation or the decreased equatorial cold-water upwelling and the redistributive warming.

In contrast to depth-integrated Eulerian heat budgets, moving to thermohaline space reveals the transport by isopycnal mixing of excess heat from the ML and seasonal thermocline across the WML base in the subtropical Atlantic. The absorption of this isopycnal flux generates strong spice warming around and below the WML base that contributes to the along-isopycnal warming and salinification of the shallow tropical Atlantic as opposed to the freshening of the Indo-Pacific. This excess heat within the ML results from the redistribution feedback, which partly compensates the redistributive cooling that is responsible for an unexpected subtropical decreased stratification and deepening mixed layer in the tropical Atlantic. Warming by spice captures the excess heat at the WML base north of 20°S in the subtropical Atlantic. However, it remains within the shallowest 500 m without contributing much to the warming of the depth-integrated heat by spice and it should transfer into warming by heave once diapycnally diffused in the ocean interior.

The adiabatic mid-depth cell that outcrops in the high-latitude regions (stably stratified in salinity) has a strong along-isopycnal flow that transports excess heat downward by advection and isopycnal mixing. Also, the reduced convection at high latitudes (60°N/S) by surface warming reduces the along-isopycnal deep heat loss, which primarily contributes to the redistributed warming captured by the warming by spice. Warming by spice can thus result from the accumulation and sequestration of deep heat by redistribution, indirectly resulting from surface buoyancy forcing.

APPENDIX

Projection of the Transformation Vector in Spice and Heave

This appendix presents how transformation vectors **J** given in S–θ space (section 2c) can be projected in σ–χ space along isopycnals σ and along S–θ curves (denoted χ) to provide the contribution of **J** onto spice and heave (section 2b). Such projection (Fig. A1) reveals which process of the heat and salt budgets predominantly contributes to alter the spice and heave components of temperature and salinity anomalies. The isopycnal angle Ω_σ is retrieved from $\tan(\Omega_\sigma) = J^\theta_{\text{spice}}/J^S_{\text{spice}} = -[\alpha_0(\partial\sigma/\partial S)]/[\beta_0(\partial\sigma/\partial\theta)]$ and the angle of the S–θ curve, Ω_χ, follows $\tan(\Omega_\chi) = J^\theta_{\text{heave}}/J^S_{\text{heave}} = [\alpha_0(\partial\theta/\partial z)]/[\beta_0(\partial S/\partial z)]$ when using a normalization by the domain-averaged thermal expansion coefficient $(\alpha_0 = -\rho^{-1}\partial\rho/\partial\theta)$ and saline contraction coefficient $(\beta_0 = \rho^{-1}\partial\rho/\partial S)$ as in Huang et al. (2021). The transformation vector **J** in S–θ space (J^S, J^θ) is projected in σ–χ space $(\mathbf{J}_{\text{spice}}, \mathbf{J}_{\text{heave}})$:

$$J^S = J^S_{\text{spice}} + J^S_{\text{heave}}, \tag{A1}$$

$$J^\theta = J^\theta_{\text{spice}} + J^\theta_{\text{heave}} = J^S_{\text{spice}}\left(-\alpha_0\frac{\partial\sigma}{\partial S}\bigg/\beta_0\frac{\partial\sigma}{\partial\theta}\right) + J^S_{\text{heave}}\left(\alpha_0\frac{\partial\theta}{\partial z}\bigg/\beta_0\frac{\partial S}{\partial z}\right), \tag{A2}$$

$$\begin{pmatrix} J^S \\ J^\theta \end{pmatrix} = \hat{J}^S_{\text{spice}}\begin{pmatrix} \beta_0\partial\sigma/\partial\theta \\ -\alpha_0\partial\sigma/\partial S \end{pmatrix} + \hat{J}^S_{\text{heave}}\begin{pmatrix} \beta_0\partial S/\partial z \\ \alpha_0\partial\theta/\partial z \end{pmatrix}. \tag{A3}$$

By introducing $\hat{J}^S_{\text{spice}} = \mathbf{J}^S_{\text{spice}}(\beta_0\partial\sigma/\partial\theta)^{-1}$ and $\hat{J}^S_{\text{heave}} = \mathbf{J}^S_{\text{heave}}(\beta_0\partial S/\partial z)^{-1}$, this linear system becomes

$$\begin{pmatrix} J^S \\ J^\theta \end{pmatrix} = \begin{pmatrix} \beta_0\partial\sigma/\partial\theta & \beta_0\partial S/\partial z \\ -\alpha_0\partial\sigma/\partial S & \alpha_0\partial\theta/\partial z \end{pmatrix}\begin{pmatrix} \hat{J}^S_{\text{spice}} \\ \hat{J}^S_{\text{heave}} \end{pmatrix}, \tag{A4}$$

and after a matrix inversion

$$\begin{pmatrix} \hat{J}^S_{\text{spice}} \\ \hat{J}^S_{\text{heave}} \end{pmatrix} = \frac{1}{\alpha_0\beta_0\left(\dfrac{\partial\sigma}{\partial\theta}\dfrac{\partial\theta}{\partial z} + \dfrac{\partial\sigma}{\partial S}\dfrac{\partial S}{\partial z}\right)}\begin{pmatrix} \alpha_0\partial\theta/\partial z & -\beta_0\partial S/\partial z \\ \alpha_0\partial\sigma/\partial S & \beta_0\partial\sigma/\partial\theta \end{pmatrix}\begin{pmatrix} J^S \\ J^\theta \end{pmatrix}. \tag{A5}$$

The spice and heave components of the transformation vector are the first and second terms on the right-hand side of Eq. (A3), respectively. They are denoted $(J^S_{\text{spice}}, J^\theta_{\text{spice}})$
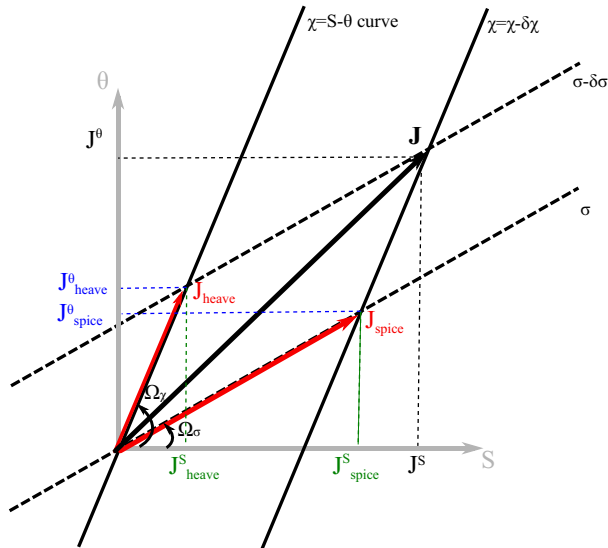
FIG. A1. Projection of the transformation vector **J** (Sv) from the S–θ space (J^S, J^θ) onto the σ–χ space (**J**$_{\text{spice}}$, **J**$_{\text{heave}}$).

and $(J^S_{\text{heave}}, J^\theta_{\text{heave}})$ in the S–θ space and can be retrieved from Eq. (A5):

$$\mathbf{J}_{\text{spice}} = \hat{J}^S_{\text{spice}} \begin{pmatrix} \beta_0 \partial\sigma/\partial\theta \\ -\alpha_0 \partial\sigma/\partial S \end{pmatrix} \mathbf{i}_\sigma = J^S_{\text{spice}}\mathbf{i}_S + J^\theta_{\text{spice}}\mathbf{i}_\theta, \quad (A6)$$

$$\mathbf{J}_{\text{heave}} = \hat{J}^S_{\text{heave}} \begin{pmatrix} \beta_0 \partial S/\partial z \\ \alpha_0 \partial\theta/\partial z \end{pmatrix} \mathbf{i}_\chi = J^S_{\text{heave}}\mathbf{i}_S + J^\theta_{\text{heave}}\mathbf{i}_\theta, \quad (A7)$$

with ($\mathbf{i}_S$, $\mathbf{i}_\theta$) and ($\mathbf{i}_\sigma$, $\mathbf{i}_\chi$), the unit vectors in the S–θ and σ–χ spaces.

REFERENCES

Armour, K. C., J. Marshall, A. Donohoe, and E. R. Newsom, 2016: Southern Ocean warming delayed by circumpolar up-welling and equatorward transport. *Nat. Geosci.*, **9**, 549–554, https://doi.org/10.1038/ngeo2731.

Banks, H. T., and J. M. Gregory, 2006: Mechanisms of ocean heat uptake in a coupled climate model and the implications for tracer based predictions of ocean heat uptake. *Geophys. Res. Lett.*, **33**, L07608, https://doi.org/10.1029/2005GL025352.

Bindoff, N. L., and T. J. McDougall, 1994: Diagnosing climate change and ocean ventilation using hydrographic data. *J. Phys. Oceanogr.*, **24**, 1137–1152, https://doi.org/10.1175/1520-0485(1994)024<1137:DCCAOV>2.0.CO;2.

Bouttes, N., J. M. Gregory, T. Kuhlbrodt, and R. S. Smith, 2014: The drivers of projected North Atlantic sea level change. *Climate Dyn.*, **43**, 1531–1544, https://doi.org/10.1007/s00382-013-1973-8.

Bronselaer, B., and L. Zanna, 2020: Heat and carbon coupling reveals ocean warming due to circulation changes. *Nature*, **584**, 227–233, https://doi.org/10.1038/s41586-020-2573-5.

Carmack, E. C., 2007: The alpha/beta ocean distinction: A perspective on freshwater fluxes, convection, nutrients and productivity in high-latitude seas. *Deep-Sea Res. II*, **54**, 2578–2598, https://doi.org/10.1016/j.dsr2.2007.08.018.

Chen, H., A. K. Morrison, C. O. Dufour, and J. L. Sarmiento, 2019: Deciphering patterns and drivers of heat and carbon storage in the Southern Ocean. *Geophys. Res. Lett.*, **46**, 3359–3367, https://doi.org/10.1029/2018GL080961.

Cheng, L., K. E. Trenberth, J. Fasullo, T. Boyer, J. Abraham, and J. Zhu, 2017: Improved estimates of ocean heat content from 1960 to 2015. *Sci. Adv.*, **3**, e1601545, https://doi.org/10.1126/sciadv.1601545.

Church, J. A., J. S. Godfrey, D. R. Jackett, and T. J. McDougall, 1991: A model of sea level rise caused by ocean thermal extension. *J. Climate*, **4**, 438–456, https://doi.org/10.1175/1520-0442(1991)004<0438:AMOSLR>2.0.CO;2.

——, and Coauthors, 2011: Revisiting the Earth's sea-level and energy budgets from 1961 to 2008. *Geophys. Res. Lett.*, **38**, L18601, https://doi.org/10.1029/2011GL048794.

Clément, L., E. L. McDonagh, A. Marzocchi, and A. J. G. Nurser, 2020: Signature of ocean warming at the mixed layer base. *Geophys. Res. Lett.*, **47**, e2019GL086269, https://doi.org/10.1029/2019GL086269.

Dias, F. B., and Coauthors, 2020: Ocean heat storage in response to changing ocean circulation processes. *J. Climate*, **33**, 9065–9082, https://doi.org/10.1175/JCLI-D-19-1016.1.

Doney, S. C., S. Yeager, G. Danabasoglu, W. G. Large, and J. C. McWilliams, 2007: Mechanisms governing interannual variability of upper-ocean temperature in a global ocean hindcast simulation. *J. Phys. Oceanogr.*, **37**, 1918–1938, https://doi.org/10.1175/JPO3089.1.

Döös, K., J. Nilsson, J. Nycander, L. Brodeau, and M. Ballarotta, 2012: The world ocean thermohaline circulation. *J. Phys. Oceanogr.*, **42**, 1445–1460, https://doi.org/10.1175/JPO-D-11-0163.1.

Durack, P. J., and S. E. Wijffels, 2010: Fifty-year trends in global ocean salinities and their relationship to broad-scale warming. *J. Climate*, **23**, 4342–4362, https://doi.org/10.1175/2010JCLI3377.1.

Emery, W. J., 2001: Water types and water masses. *Encyclopedia of Ocean Sciences*, Vol. 6, Elsevier Science, 3179–3187, https://doi.org/10.1006/rwos.2001.0108.

Exarchou, E., T. Kuhlbrodt, J. M. Gregory, and R. S. Smith, 2015: Ocean heat uptake processes: A model intercomparison. *J. Climate*, **28**, 887–908, https://doi.org/10.1175/JCLI-D-14-00235.1.

Ferrari, R., and D. Ferreira, 2011: What processes drive the ocean heat transport? *Ocean Modell.*, **38**, 171–186, https://doi.org/10.1016/j.ocemod.2011.02.013.

Gao, L., S. R. Rintoul, and W. Yu, 2018: Recent wind-driven change in Subantarctic Mode Water and its impact on ocean heat storage. *Nat. Climate Change*, **8**, 58–63, https://doi.org/10.1038/s41558-017-0022-8.

Garuba, O. A., and B. A. Klinger, 2016: Ocean heat uptake and interbasin transport of the passive and redistributive components of surface heating. *J. Climate*, **29**, 7507–7527, https://doi.org/10.1175/JCLI-D-16-0138.1.

Gent, P. R., and J. C. McWilliams, 1990: Isopycnal mixing in ocean circulation models. *J. Phys. Oceanogr.*, **20**, 150–155, https://doi.org/10.1175/1520-0485(1990)020<0150:IMIOCM>2.0.CO;2.

Gordon, C., C. Cooper, C. A. Senior, H. Banks, J. M. Gregory, T. C. Johns, J. F. B. Mitchell, and R. A. Wood, 2000: The simulation of SST, sea ice extents and ocean heat transports in a version of the Hadley Centre coupled model without

flux adjustments. *Climate Dyn.*, **16**, 147–168, https://doi.org/10.1007/s003820050010.

Gregory, J. M., 2000: Vertical heat transports in the ocean and their effect on time-dependent climate change. *Climate Dyn.*, **16**, 501–515, https://doi.org/10.1007/s003820000059.

——, and Coauthors, 2016: The Flux-Anomaly-Forced Model Intercomparison Project (FAFMIP) contribution to CMIP6: Investigation of sea-level and ocean climate change in response to CO_2 forcing. *Geosci. Model Dev.*, **9**, 3993–4017, https://doi.org/10.5194/gmd-9-3993-2016.

——, T. Andrews, P. Ceppi, T. Mauritsen, and M. J. Webb, 2020: How accurately can the climate sensitivity to CO_2 be estimated from historical climate change? *Climate Dyn.*, **54**, 129–157, https://doi.org/10.1007/s00382-019-04991-y.

Griffies, S. M., A. Gnanadesikan, R. C. Pacanowski, V. D. Larichev, J. K. Dukowicz, and R. D. Smith, 1998: Isoneutral diffusion in a *z*-coordinate ocean model. *J. Phys. Oceanogr.*, **28**, 805–830, https://doi.org/10.1175/1520-0485(1998)028<0805:IDIAZC>2.0.CO;2.

Groeskamp, S., J. D. Zika, T. J. McDougall, B. M. Sloyan, and F. Laliberté, 2014: The representation of ocean circulation and variability in thermodynamic coordinates. *J. Phys. Oceanogr.*, **44**, 1735–1750, https://doi.org/10.1175/JPO-D-13-0213.1.

Häkkinen, S., P. B. Rhines, and D. L. Worthen, 2015: Heat content variability in the North Atlantic Ocean in ocean reanalyses. *Geophys. Res. Lett.*, **42**, 2901–2909, https://doi.org/10.1002/2015GL063299.

——, ——, and ——, 2016: Warming of the global ocean: Spatial structure and water mass trends. *J. Climate*, **29**, 4949–4963, https://doi.org/10.1175/JCLI-D-15-0607.1.

Hieronymus, M., J. Nilsson, and J. Nycander, 2014: Water mass transformation in salinity–temperature space. *J. Phys. Oceanogr.*, **44**, 2547–2568, https://doi.org/10.1175/JPO-D-13-0257.1.

Holmes, R. M., J. D. Zika, and M. H. England, 2019: Diathermal heat transport in a global ocean model. *J. Phys. Oceanogr.*, **49**, 141–161, https://doi.org/10.1175/JPO-D-18-0098.1.

Huang, R. X., L. S. Yu, and S. Q. Zhou, 2021: Quantifying climate signals: Spicity, orthogonality, and distance. *J. Geophys. Res.*, **126**, e2020JC016646, https://doi.org/10.1029/2020JC016646.

Khatiwala, S. P., and Coauthors, 2013: Global ocean storage of anthropogenic carbon. *Biogeosciences*, **10**, 2169–2191, https://doi.org/10.5194/bg-10-2169-2013.

Kraus, E. B., and J. S. Turner, 1967: A one-dimensional model of the seasonal thermocline II. The general theory and its consequences. *Tellus*, **19**, 98–106, https://doi.org/10.3402/tellusa.v19i1.9753.

Kuhlbrodt, T., and J. M. Gregory, 2012: Ocean heat uptake and its consequences for the magnitude of sea level rise and climate change. *Geophys. Res. Lett.*, **39**, L18608, https://doi.org/10.1029/2012GL052952.

——, ——, and L. C. Shaffrey, 2015: A process-based analysis of ocean heat uptake in an AOGCM with an eddy-permitting ocean component. *Climate Dyn.*, **45**, 3205–3226, https://doi.org/10.1007/s00382-015-2534-0.

Lago, V., S. E. Wijffels, P. J. Durack, J. A. Church, N. L. Bindoff, and S. J. Marsland, 2016: Simulating the role of surface forcing on observed multidecadal upper ocean salinity changes. *J. Climate*, **29**, 5575–5588, https://doi.org/10.1175/JCLI-D-15-0519.1.

Levang, S. J., and R. W. Schmitt, 2015: Centennial changes of the global water cycle in CMIP5 models. *J. Climate*, **28**, 6489–6502, https://doi.org/10.1175/JCLI-D-15-0143.1.

——, and ——, 2020: What causes the AMOC to weaken in CMIP5? *J. Climate*, **33**, 1535–1545, https://doi.org/10.1175/JCLI-D-19-0547.1.

Levitus, S., et al., 2012: World ocean heat content and thermosteric sea level change (0–2000 m), 1955–2010. *Geophys. Res. Lett.*, **39**, L10603, https://doi.org/10.1029/2012GL051106.

Lowe, J. A., and J. M. Gregory, 2006: Understanding projections of sea level rise in a Hadley Centre coupled climate model. *J. Geophys. Res.*, **111**, C11014, https://doi.org/10.1029/2005JC003421.

Lozier, M. S., and Coauthors, 2019: A sea change in our view of overturning in the subpolar North Atlantic. *Science*, **363**, 516–521, https://doi.org/10.1126/science.aau6592.

Luyten, J. R., J. Pedlosky, and H. Stommel, 1983: The ventilated thermocline. *J. Phys. Oceanogr.*, **13**, 292–309, https://doi.org/10.1175/1520-0485(1983)013<0292:TVT>2.0.CO;2.

Manabe, S., K. Bryan, and M. J. Spelman, 1990: Transient response of a global ocean–atmosphere model to a doubling of atmospheric carbon dioxide. *J. Phys. Oceanogr.*, **20**, 722–749, https://doi.org/10.1175/1520-0485(1990)020<0722:TROAGO>2.0.CO;2.

Marshall, J., and K. Speer, 2012: Closure of the meridional overturning circulation through Southern Ocean upwelling. *Nat. Geosci.*, **5**, 171–180, https://doi.org/10.1038/ngeo1391.

——, J. R. Scott, K. C. Armour, J. M. Campin, M. Kelley, and A. Romanou, 2015: The ocean's role in the transient response of climate to abrupt greenhouse gas forcing. *Climate Dyn.*, **44**, 2287–2299, https://doi.org/10.1007/s00382-014-2308-0.

Mauritzen, C., A. Melsom, and R. T. Sutton, 2012: Importance of density-compensated temperature change for deep North Atlantic Ocean heat uptake. *Nat. Geosci.*, **5**, 905–910, https://doi.org/10.1038/ngeo1639.

Morrison, A. K., S. M. Griffies, M. Winton, W. G. Anderson, and J. L. Sarmiento, 2016: Mechanisms of Southern Ocean heat uptake and transport in a global eddying climate model. *J. Climate*, **29**, 2059–2075, https://doi.org/10.1175/JCLI-D-15-0579.1.

Munk, W., and C. Wunsch, 1998: Abyssal recipes II: Energetics of tidal and wind mixing. *Deep-Sea Res.*, **45**, 1977–2010, https://doi.org/10.1016/S0967-0637(98)00070-3.

Nurser, A. J. G., R. Marsh, and R. G. Williams, 1999: Diagnosing water mass formation from air–sea fluxes and surface mixing. *J. Phys. Oceanogr.*, **29**, 1468–1487, https://doi.org/10.1175/1520-0485(1999)029<1468:DWMFFA>2.0.CO;2.

Pacanowski, R. C., and S. G. H. Philander, 1981: Parameterization of vertical mixing in numerical models of tropical oceans. *J. Phys. Oceanogr.*, **11**, 1443–1451, https://doi.org/10.1175/1520-0485(1981)011<1443:POVMIN>2.0.CO;2.

Rahmstorf, S., 1993: A fast and complete convection scheme for ocean models. *Ocean Modell.*, **101**, 9–11.

Rayner, N. A., D. E. Parker, E. B. Horton, C. K. Folland, L. V. Alexander, D. P. Rowell, E. C. Kent, and A. Kaplan, 2003: Global analyses of sea surface temperature, sea ice, and night marine air temperature since the late nineteenth century. *J. Geophys. Res.*, **108**, 4407, https://doi.org/10.1029/2002JD002670.

Redi, M. H., 1982: Oceanic isopycnal mixing by coordinate rotation. *J. Phys. Oceanogr.*, **12**, 1154–1158, https://doi.org/10.1175/1520-0485(1982)012<1154:OIMBCR>2.0.CO;2.

Rhein, M., and Coauthors, 2013: Observations: Ocean. *Climate Change 2013: The Physical Science Basis*, T. F. Stocker et al., Eds., Cambridge University Press, 255–316 pp., https://doi.org/10.1017/CBO9781107415324.010.

Rintoul, S. R., and M. H. England, 2002: Ekman transport dominates local air–sea fluxes in driving variability of Subantarctic

Mode Water. *J. Phys. Oceanogr.*, **32**, 1308–1321, https://doi. org/10.1175/1520-0485(2002)032<1308:ETDLAS>2.0.CO;2.

Saenko, O. A., J. C. Fyfe, and M. H. England, 2005: On the response of the oceanic wind-driven circulation to atmospheric CO_2 increase. *Climate Dyn.*, **25**, 415–426, https://doi.org/10. 1007/s00382-005-0032-5.

——, J. M. Gregory, S. M. Griffies, M. P. Couldrey, and F. B. Dias, 2021: Contribution of ocean physics and dynamics at different scales to heat uptake in low-resolution AOGCMs. *J. Climate*, **34**, 2017–2035, https://doi.org/10.1175/JCLI-D-20-0652.1.

Speer, K. G., 1993: Conversion among North Atlantic surface water types. *Tellus*, **45A**, 72–79, https://doi.org/10.3402/tellusa. v45i1.14858.

——, and E. Tziperman, 1992: Rates of water mass formation in the North Atlantic Ocean. *J. Phys. Oceanogr.*, **22**, 93–104, https://doi.org/10.1175/1520-0485(1992)022<0093:ROWMFI>2. 0.CO;2.

Stommel, H. M., 1979: Determination of water mass properties of water pumped down from Ekman layer to the geostrophic flow below. *Proc. Natl. Acad. Sci. USA*, **76**, 3051–3055, https:// doi.org/10.1073/pnas.76.7.3051.

Talley, L. D., 2013: Closure of the global overturning circulation through the Indian, Pacific, and Southern Oceans: Schematics and transports. *Oceanography*, **26**, 80–97, https://doi.org/10. 5670/oceanog.2013.07.

Tett, S. F. B., J. M. Gregory, N. Freychet, C. Cartis, M. J. Mineter, and L. Roberts, 2022: Does model calibration reduce uncertainty in climate projections? *J. Climate*, **35**, 2585–2602, https://doi.org/10.1175/JCLI-D-21-0434.1.

Visbeck, M., J. Marshall, T. Haine, and M. Spall, 1997: Specification of eddy transfer coefficients in coarse-resolution ocean circulation models. *J. Phys. Oceanogr.*, **27**, 381–402, https:// doi.org/10.1175/1520-0485(1997)027<0381:SOETCI>2.0.CO;2.

Walin, G., 1982: On the relation between sea-surface heat flow and thermal circulation in the ocean. *Tellus*, **34**, 187–195, https://doi.org/10.3402/tellusa.v34i2.10801.

Williams, R. G., V. Roussenov, D. Smith, and M. S. Lozier, 2014: Decadal evolution of ocean thermal anomalies in the North Atlantic: The effects of Ekman, overturning, and horizontal transport. *J. Climate*, **27**, 698–719, https://doi.org/10.1175/ JCLI-D-12-00234.1.

Winton, M., S. M. Griffies, B. L. Samuels, J. L. Sarmiento, and T. L. Frölicher, 2013: Connecting changing ocean circulation with changing climate. *J. Climate*, **26**, 2268–2278, https://doi. org/10.1175/JCLI-D-12-00296.1.

Wong, A. P. S., N. L. Bindoff, and J. A. Church, 1999: Large-scale freshening of intermediate waters in the Pacific and Indian Oceans. *Nature*, **400**, 440–443, https://doi.org/10.1038/22733.

Xie, P., and G. K. Vallis, 2012: The passive and active nature of ocean heat uptake in idealized climate change experiments. *Climate Dyn.*, **38**, 667–684, https://doi.org/10.1007/s00382-011-1063-8.

Yin, J., S. Griffies, and R. J. Stouffer, 2010: Spatial variability of sea-level rise in twenty-first-century projections. *J. Climate*, **23**, 4585–4607, https://doi.org/10.1175/2010JCLI3533.1.

Zanna, L., S. Khatiwala, J. M. Gregory, J. Ison, and P. Heimbach, 2019: Global reconstruction of historical ocean heat storage and transport. *Proc. Natl. Acad. Sci. USA*, **116**, 1126–1131, https://doi.org/10.1073/pnas.1808838115.

Zhu, C., and Z. Liu, 2020: Weakening Atlantic overturning circulation causes South Atlantic salinity pile-up. *Nat. Climate Change*, **10**, 998–1003, https://doi.org/10.1038/s41558-020-0897-7.

Zika, J. D., M. H. England, and W. P. Sijp, 2012: The ocean circulation in thermohaline coordinates. *J. Phys. Oceanogr.*, **42**, 708–724, https://doi.org/10.1175/JPO-D-11-0139.1.

——, J. M. Gregory, E. L. McDonagh, A. Marzocchi, and L. Clément, 2021: Recent water mass changes reveal mechanisms of ocean warming. *J. Climate*, **34**, 3461–3479, https:// doi.org/10.1175/JCLI-D-20-0355.1.

Zou, S., M. S. Lozier, F. Li, R. Abernathey, and L. Jackson, 2020: Density-compensated overturning in the Labrador Sea. *Nat. Geosci.*, **13**, 121–126, https://doi.org/10.1038/s41561-019-0517-1.